

NONEQUILIBRIUM RADIATION AND CHEMISTRY MODELS FOR  
AEROCAPTURE VEHICLE FLOWFIELDS

39P



# aerospace engineering department

Semiannual Progress Report

January 1993--June 1993

## TEXAS A&M UNIVERSITY

TAMRF Report No. 6382-93-02  
September 1993

NASA Grant No. NAG-1-1003

Leland A. Carlson  
Professor of Aerospace Engineering  
Texas A&M University  
College Station, TX 77843-3141

(NASA-CR-194645) NONEQUILIBRIUM  
RADIATION AND CHEMISTRY MODELS FOR  
AEROCAPTURE VEHICLE FLOWFIELDS  
Semiannual Progress Report, Jan. -  
Jun. 1993 (Texas A&M Univ.) 39 p

N94-17095

Unclass

G3/34 0191735

TEXAS ENGINEERING EXPERIMENT STATION

**NONEQUILIBRIUM RADIATION AND CHEMISTRY MODELS FOR  
AEROCAPTURE VEHICLE FLOWFIELDS**

**Semiannual Progress Report**

January 1993--June 1993

TAMRF Report No. 6382-93-02  
September 1993

NASA Grant No. NAG-1-1003

Leland A. Carlson  
Professor, Aerospace Engineering Department  
Texas A&M University  
College Station, TX 77843-3141

# **NONEQUILIBRIUM RADIATION AND CHEMISTRY MODELS FOR AEROCAPTURE VEHICLE FLOWFIELDS**

## **I. Introduction**

This report covers approximately the period from January 1993 thru August 1993. The primary tasks during this period have been the development of a single and multi-vibrational temperature preferential vibration-dissociation coupling model, the development of a normal shock nonequilibrium radiation-gasdynamic coupling model based upon the blunt body model, and the comparison of results obtained with these models with experimental data. In addition, an extensive series of computations were conducted using the blunt body model to develop a set of reference results covering a wide range of vehicle sizes, altitudes, and entry velocities.

## **II. Personnel**

The staff associated with this project during the present reporting period have been Dr. Leland A. Carlson, Principal Investigator, Dr. Thomas A. Gally, Visiting Assistant Professor, and Mr. David Mott and Mr. David McGough, Graduate Research Assistants. Dr. Gally has been primarily associated with the development of the nonequilibrium chemical and radiation models, multi-component diffusion models, and the radiation coupled nonequilibrium multi-temperature viscous shock layer code. During this reporting period he has conducted a series of computations which cover nonequilibrium re-entry heating conditions for a wide variety of entry flight conditions. Mr. McGough has developed a preferential vibration-dissociation version of the forebody code which can be used in either a single or multi-vibrational temperature mode and has compared results obtained with Fire 2 flight data. Mr. McGough was supported by the project through August 1993 and plans to receive his masters' degree in December 1993. Mr. Mott has developed a normal shock version of the blunt body code that includes nonequilibrium radiative coupling and has compared the code predictions with available shock tube data. Mr. Mott, who was supported by an ONR-ASEE fellowship has left Texas A&M to pursue his Ph.D. at the University of Michigan. He also plans to receive his masters' degree in December 1993.

## **III. Discussion of Research Effort**

During this reporting period, the viscous shock layer nonequilibrium chemistry and radiation blunt body program was applied to a wide range of flight conditions on vehicles. These results, which utilized eleven species and over twenty-six chemical reactions, were for 60 degree sphere cone bodies having nose radii from 0.5 m to 2.3 m and included velocities from nine to sixteen km/sec and altitudes from 70 to 80 km. Comparison of the results with equilibrium analyses indicates that the net effect of nonequilibrium and in particular atomic LTNE in the bow shock layer is to

reduce the total radiative heat load to the vehicle surface. There is also an indication in the results that at the lower velocities that molecular LTNE may enhance the nonequilibrium radiation. However, this conclusion does depend upon the accuracy of the radiation model for molecular species, particularly  $N_2^+$ , and is under investigation. The results of this survey are presented and discussed in AIAA Paper 93-3230, which was presented at the AIAA 24th Plasmadynamics and Lasers Conference in July 1993. A copy of this paper is included as an appendix of this report.

The work associated with the development of a preferential vibration dissociation coupling model was essentially divided into two parts. In the first portion of the study, the model, following the original blunt body model, assumed a single vibrational temperature for all diatomic species. Results obtained with this new preferential model demonstrated that preferential behavior did, as expected, increase the size of the nonequilibrium zone behind the bow shock layer. However, comparisons with Fire 2 flight measurements indicated better agreement with the original nonpreferential model. Specifically, a preferential temperature of  $U = D/3k$  appeared to introduce too large an amount of preferential behavior into the solution for the Fire 2 cases. This addition led to larger regions of nonequilibrium and  $N_2^+$  concentrations, which significantly increased the amount of molecular radiation. Preferential solutions were also obtained using modified absorption coefficients for various molecular bands, in particular the  $N_2^+(1-)$  and the  $N_2$  first and second positive bands. While comparisons with Fire 2 flight measurements for these measurements were better than the previous preferential results, the nonpreferential computations still matched the flight data better. Apparently, additional investigations of the modeling of  $N_2^+(1-)$  band may be needed, particularly since this band always appears to be very near LTE and is the only band with this characteristic.

In summary, these single vibrational temperature preferential studies indicate that preferential behavior, if it exists, is probably small. Since many current methods of treating vibration-dissociation coupling introduce approximations which effectively introduce preferential behavior, in some cases significant amounts, this conclusion may explain why several other models significantly over-predict the Fire 2 radiative heating data. Based upon the present studies, it would appear that the appropriate value for the preferential temperature in a preferential model would be on the order of  $D/k$  or  $3D/k$ . Results from these studies were presented at the AIAA 24th Plasmadynamics and Lasers Conference in July 1993 as AIAA Paper 93-3197. This paper is also included as an appendix of this report. Interestingly, after this paper was presented, Dr. Charles Treanor commented that he recalls unpublished studies which indicated that perhaps the appropriate value for the preferential temperature was  $3D/k$  instead of the suggested published values of  $D/3k$  and  $D/6k$ .

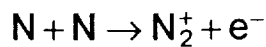
The second portion of the vibration-dissociation studies involved the examination of the effect of using multiple vibrational temperatures. Thus, the

preferential model described previously was modified to permit each diatomic species to have its own vibrational temperature. In addition, unlike the blunt body single vibrational temperature model, vibrational-electron coupling was only assumed to exist between  $N_2$  and free electrons. However, no vibration-vibration coupling was assumed to take place. Thus, comparison of results obtained with this model with the previous single vibrational temperature model, which inherently assumes extensive vibrational-vibrational coupling, should indicate whether or not vibration-vibration coupling significantly affects nonequilibrium radiative heat transfer phenomena.

Results have been obtained using the multiple vibrational temperature model for Fire 2 cases corresponding to 1634, 1636, 1637.5, and 1639 seconds, and some typical results are shown on Figures 1 and 2. For these cases, the preferential temperature was  $6D/k$  and the original absorption coefficients were used in the radiation model. As expected, significant thermal non-equilibrium exists in the nonequilibrium region behind the shock front and also in the thermal layer near the wall. Further, as can be seen by comparison of the present Fig. 1 with Fig. 2 in AIAA Paper 93-3197 (in appendix), the translational and electron-electronic temperatures are essentially the same as the single vibrational temperature results; and the single vibrational temperature result is sort of an average of the multiple vibrational temperatures.

However, the details of the multiple vibrational temperatures are significantly different and quite interesting. First,  $O_2$  vibrationally equilibrates with the translational temperature much faster than  $N_2$ , which is expected due to the significantly faster vibrational relaxation time of  $O_2$  compared to that of  $N_2$ . Also, the  $N_2$  vibrational temperature is significantly different than the average  $T_{vib}$  and, due to vibrational electronic coupling, almost identical to the electron-electronic temperature. This result should, however, not be construed to deduce that it is always adequate to assume that  $T_{vib}$  and  $T_{e-elec}$  are the same since, as shown previously by Gally, Carlson, and Green that such an assumption can in some cases lead to errors in both  $T_{vib}$  and  $T_e$ . Conversely, these and previous results do not mean that the  $T_e = T_{vib}$  is a bad assumption. In many cases, it probably is adequate, considering our present lack of knowledge concerning some of the key radiation parameters. However, it is believed that it is "better" to use at least a three temperature model when possible.

Finally, the multiple vibrational results show that the vibrational temperatures for  $N_2^+$ ,  $NO$ ,  $NO^+$ , and  $O_2^+$  all equilibrate very rapidly with the translational temperature in the immediate post shock nonequilibrium zone. This behavior is in agreement with previous results obtain by Carlson and Rieper using the Cornell Aeronautical Lab Normal Shock Program with multiple vibration temperatures and is probably indicative of the fact that these species are primarily formed in the post-shock front zone by atom-atom combination. For example, in the case of  $N_2^+$ , the primary reaction forming  $N_2^+$  is



Since in this case  $\text{N}_2^+$  is formed from two translating atoms, it seems intuitively logical that the resulting characteristic vibrational energy should be associated with the translational temperature and not the vibrational energy of  $\text{N}_2$ . Again, it should be noted that these results do not include vibration-vibration coupling.

In the thermal region near the wall, most of the individual species' vibrational temperatures appear to closely follow the translational temperature. In this zone, the  $T_{v,o_2}$  falls below the other temperatures; and at first, this result appears peculiar. However, the  $\text{O}_2$  concentration gradient is very negative near the wall (i.e.  $\text{O}_2$  is rapidly increasing as the wall is approached). Consequently,  $\text{O}_2$  molecules are formed near the wall at relatively low vibrational and translational temperatures and then, due to the concentration gradients, diffuse away from the wall, creating a region of lower oxygen vibrational temperatures.

While not shown in this report, similar temperature and concentration profile results have been obtained at the other Fire 2 flight data point conditions. In addition, results have also been obtained in which all absorption coefficients have been modified based upon the results of Laux, Moreau, and Kruger. Radiative heat transfer results for these cases, along with the other results, are shown in Tables I to IV for the wavelength regions measured in the Fire 2 experiments. While some changes are apparent in these values, if they were plotted on a logarithmic scale as in AIAA Paper 93-3197, the differences are quite small. Thus, it appears that while modified absorption coefficients do seemingly improve the results, vibrational preferential behavior and/or multiple vibrational temperatures seem to have little affect on the radiative heating. Tables showing these results are presented below.

Time (sec)	$Q_{r,}$ (2-4eV)	$Q_{r,}$ 0-6.2eV	$Q_r$ Absorbed	$Q_c$	Q Total watts/cm <sup>2</sup>	$\Delta$ cm
1,634	5.78	8.31	10.87	187.9	198.77	5.21
1,636	7.96	20.03	42.71	274.46	317.17	4.64
1,637.5	10.77	39.64	90.76	352.17	442.93	4.51
1,639	15.92	74.69	160.7	444.49	605.19	4.47
1,640.5	24.54	125.24	242.4	541.35	783.75	4.47

Table I -- Fire 2 Radiative Heat Transfer Predictions  
Single Vibrational Temperature Case  
 $U = 6D/k$ , Original Absorption Coefficients

Time (sec)	$Q_r$ (2-4eV)	$Q_r$ 0-6.2eV	$Q_r$ Absorbed	$Q_c$	Q Total watts/cm <sup>2</sup>	$\Delta$ cm
1,634	5.26	7.9	11.01	188.44	199.45	5.24
1,636	7.26	19.33	42.34	274.94	317.28	4.64
1,637.5	10.06	39.61	92.78	350.92	443.7	4.53
1,639	14.87	73.54	160.2	444.36	604.57	4.47
1,640.5	23.08	123.2	238.9	536.88	775.78	4.47

Table II -- Fire 2 Radiative Heat Transfer Predictions  
Single Vibrational Temperature Case  
 $U = 6D/k$ ,  $N_2$  and  $N_2^+$  Absorption Coefficients Modified

Time (sec)	$Q_r$ (2-4eV)	$Q_r$ 0-6.2eV	$Q_r$ Absorbed	$Q_c$	Q Total watts/cm <sup>2</sup>	$\Delta$ cm
1,634	5.26	7.9	11	188.43	199.43	5.24
1,636	7.4	20.17	45.47	275.35	320.82	4.69
1,637.5	10.05	39.64	92.78	350.91	443.68	4.53
1,639	14.92	73.63	160.3	444.33	604.63	4.47
1,640.5	23.17	123.31	238.6	535.78	774.38	4.47

Table III -- Fire 2 Radiative Heat Transfer Predictions  
Single Vibrational Temperature Case  
 $U = 6D/k$ , All Absorption Coefficients Modified

Time (sec)	$Q_r$ (2-4eV)	$Q_r$ 0-6.2eV	$Q_r$ Absorbed	$Q_c$	Q Total watts/cm <sup>2</sup>	$\Delta$ cm
1,634	6.44	8.87	10.89	187.01	197.9	5.49
1,636	9.1	21.58	45.52	273.03	318.55	4.84
1,637.5	11.96	40.74	91.44	350.94	442.38	4.62
1,639	17.17	76.02	163.8	446.12	609.92	4.55

Table IV -- Fire 2 Radiative Heat Transfer Predictions  
Multiple Vibrational Temperatures Case  
 $U = 6D/k$ , Original Absorption Coefficients

In viewing the results in the above tables, it may be noted that some of the results for the  $U = 6D/k$  case, which is essentially non-preferential vibration dissociation coupling, differ slightly from those previously presented by Gally and Carlson. The differences are due to the fact that the previous results used a variable Lewis number multi-component diffusion model while the present results use a constant Lewis number of 1.4. Complete results for the various cases and the multiple vibrational temperature studies will be contained in Mr. McGough's thesis, which will be completed during November 1993.

The other major portion of research conducted during this reporting period was associated with the development of a normal shock version of the blunt body radiating nonequilibrium viscous shock layer code. Since this report is at present quite late and since most of the normal shock work has been finished during the second half of 1993, most of the details concerning the results of this portion of the project will be reported in the next report and in the masters' thesis of David Mott. However, the results can briefly be summarized. In general, reasonable agreement has been obtained with the shock tube data of Avco at 10 km/sec and excellent agreement has been obtained with the results of Wilson in the range 9 - 12 km/sec. This latter agreement is particular important since the present model was designed to be "good" for phenomena dominated by ionization and atomic processes and the Wilson data is in this flow field regime. In addition, reasonable agreement has been obtained with the data of Sharma at NASA Ames. As stated, details of these results will be reported later.

#### **IV. Future Efforts**

During the next reporting period, the primary emphasis will be upon finishing the project. As of September 1st, all of the funds associated with the project had essentially been spent. Thus, effort during the remaining period will be upon finishing the various reports, papers, and users manuals associated with the work on this project.

#### **V. Technical Monitor**

The NASA technical monitor for this grant is Dr. Lin C. Hartung, Aerothermodynamics Branch, Space Systems Division, NASA Langley Research Center, Hampton, Virginia.

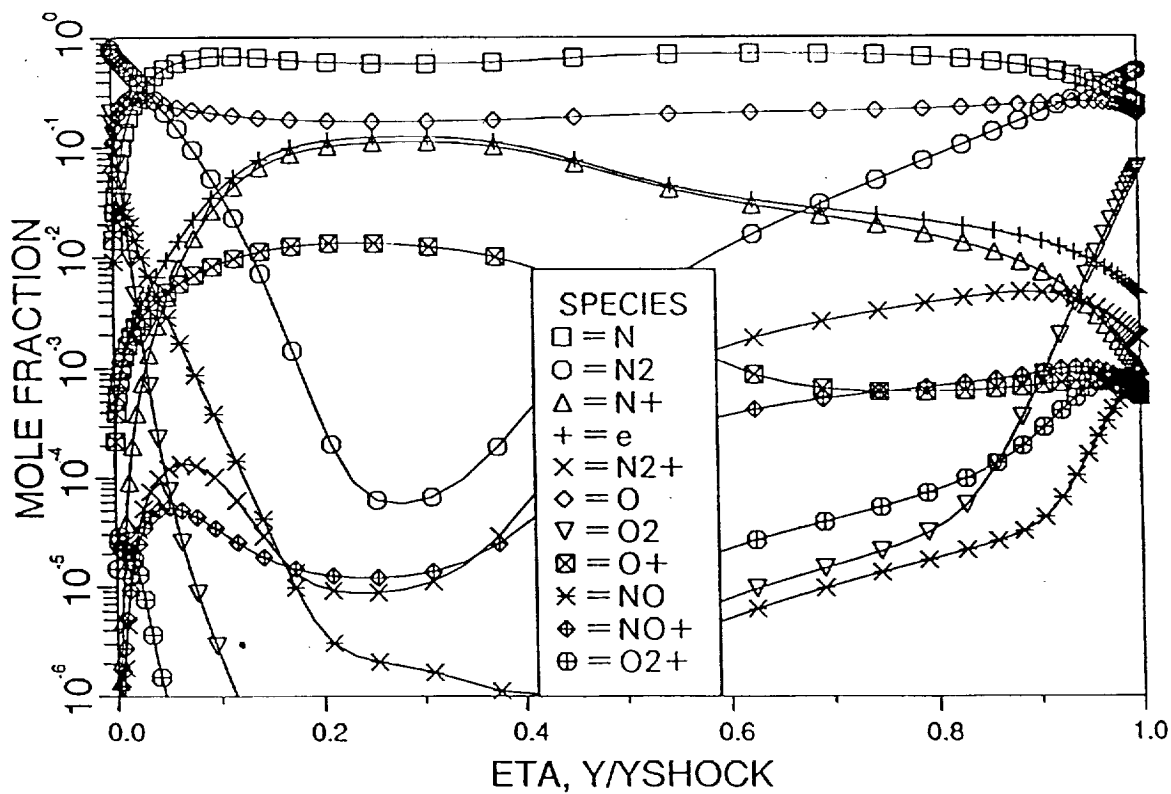
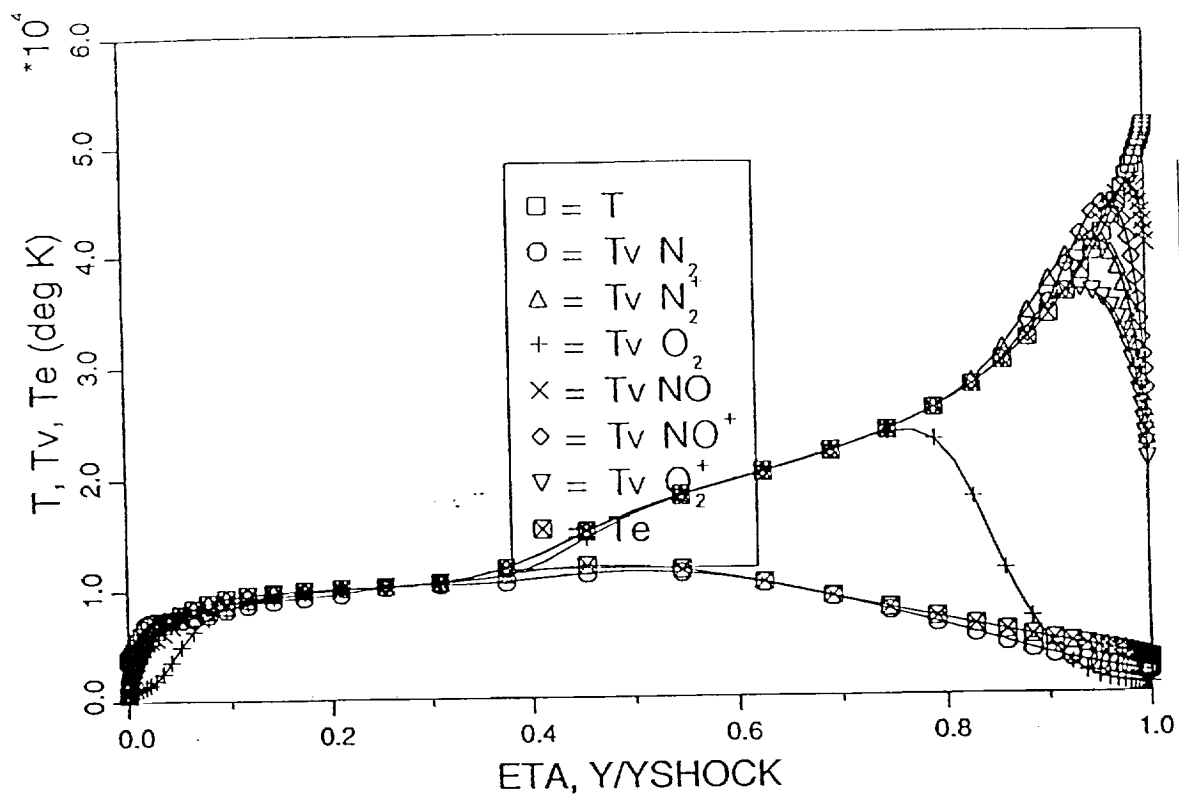
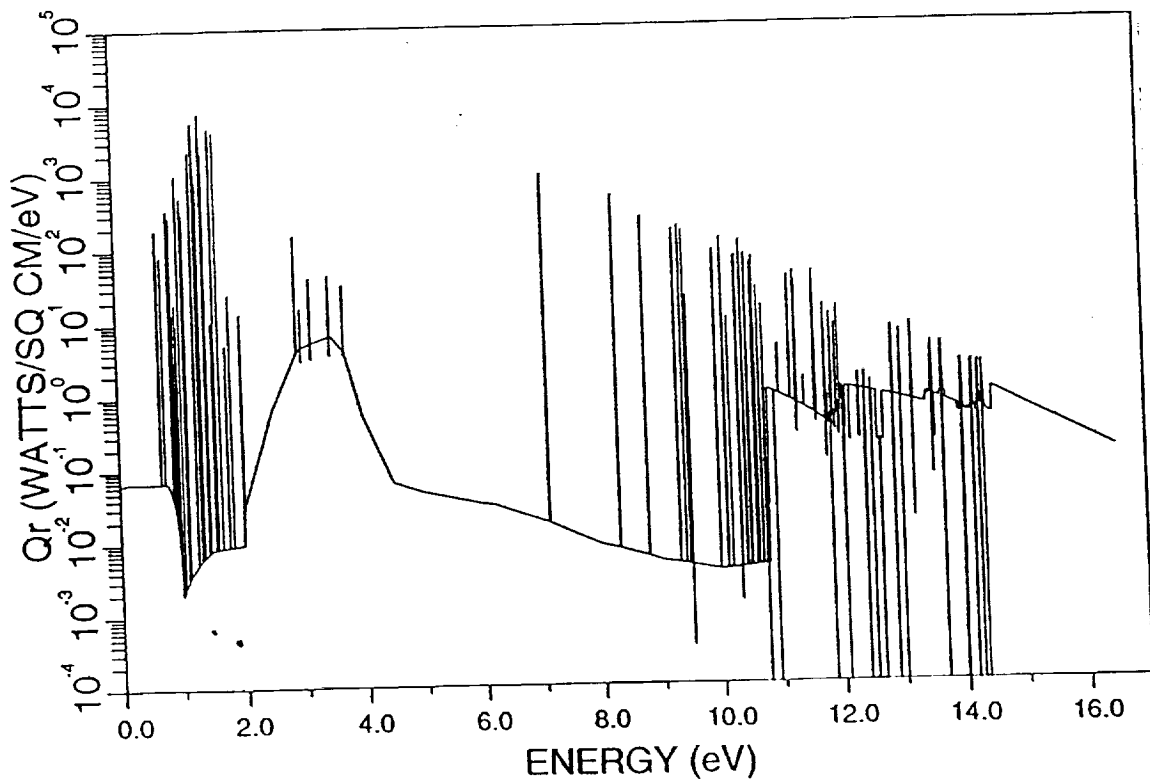
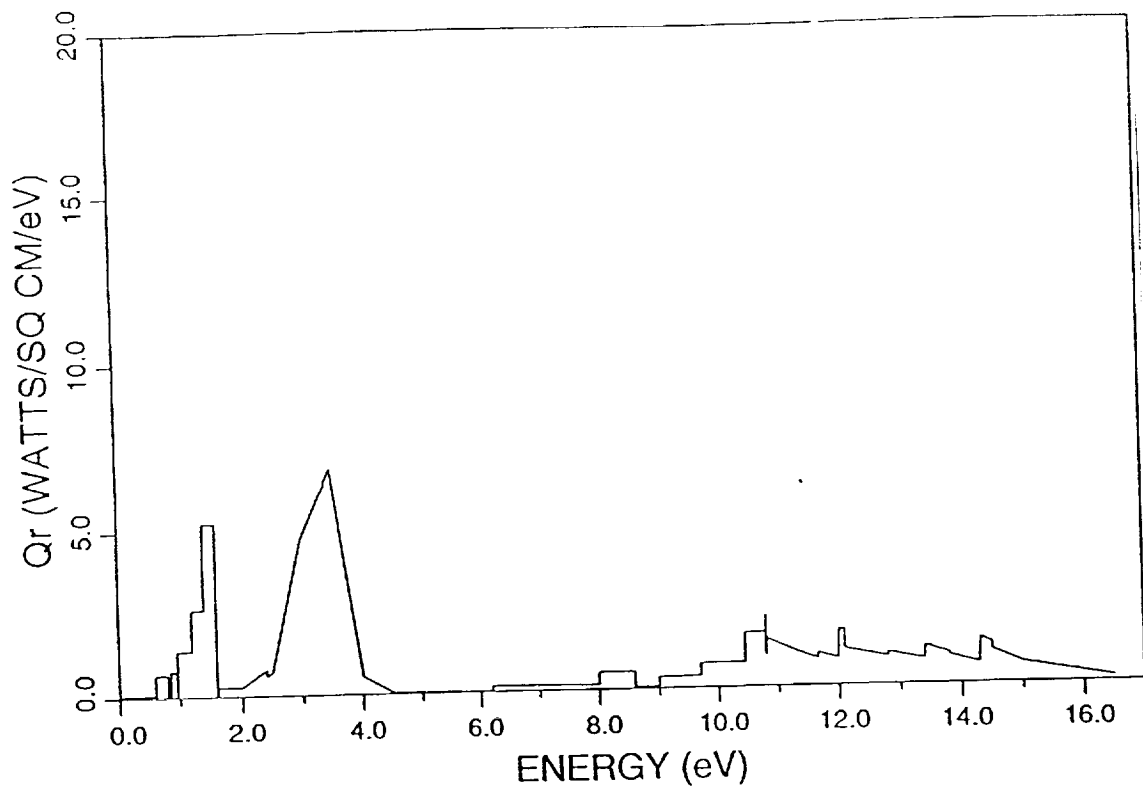


Figure 1 -- Case 1634: Air Results with  $U = 6D/k$  and Multiple Vibrational Temperatures, Temperature and Mole Fractions



**Figure 2 -- Case 1634: Air Results with  $U = 6D/k$  and Multiple Vibrational Temperatures, Grouped and Detailed Radiation Spectra**

**Appendix I**

**Survey of Nonequilibrium Re-Entry Heating for Entry Flight Conditions  
AIAA Paper 93-3230**

**by**

**Thomas A. Gally  
and  
Leland A. Carlson**

# Survey of Nonequilibrium Re-entry Heating for Entry Flight Conditions

Thomas A. Gally\*

and

Leland A. Carlson\*\*

Texas A&M University  
College Station, Texas

## Abstract

*A viscous shock layer method has been developed which includes the effects of chemical and thermal nonequilibrium and is coupled with a radiation analysis which includes thermodynamic nonequilibrium effects. This code has been used to obtain solutions for a wide variety of nonequilibrium re-entry conditions in air. The results are tabulated and displayed graphically. Comparisons are made to similar results obtained for radiatively coupled equilibrium flow and conclusions drawn on the effect of nonequilibrium and in particular thermodynamic nonequilibrium on the radiative environment about re-entry vehicles.*

## Nomenclature

$c_p$  = specific heat at constant pressure

$\dot{q}$  = heat flux

$Q$  = heat flux

$R_{\text{nose}}$  = nose radius

$S$  = distance along body

$T$  = Temperature

$W$  = curvature smoothing factor

$\Delta$  = shock standoff distance

$\kappa$  = curvature

subscripts

$c$  = convective

$e$  = electron or electronic

$j$  = sphere-cone junction

$r$  = radiative

$v$  = vibrational

$w$  = wall value

$\infty$  = freestream value

## Introduction

The proposal of a new class of re-entry vehicles in the recent past spurred the research into computational tools and theory for the calculation of nonequilibrium gas flows. The new vehicles, grouped under the general title of aero-assisted vehicles, are designed to use the upper levels of planetary atmospheres to achieve orbital/trajectory changes with a minimum expenditure of fuel. The application of such vehicles is for both interplanetary or lunar return missions and for inter-orbital runs such as between

geosynchronous and low-earth orbits. The particular interest in nonequilibrium phenomena resulted from the long duration of time these new vehicles would spend in the upper atmosphere which previous re-entry vehicles rapidly passed through on their return to the planet surface. The now defunct Aeroassisted Flight Experiment (AFE) was partially designed with the goal of providing experimental evidence for the development, calibration, and verification of the physical and numerical models involved.

In support of the research push into nonequilibrium flows, the authors pursued the development of numerical tools for the rapid and accurate calculation of nonequilibrium effects (see Refs. 1-5). Attempts were made to use existing theories and methods in an integrated package which could be used for routine engineering analysis of re-entry flight conditions. The effects of chemical, thermal, and thermodynamic nonequilibrium along with radiative-gasdynamics coupling have been modeled in the single resulting program.

This paper provides a summary of this research effort with cited references for the interested reader to pursue. A survey of results for a diverse series of flight conditions and body sizes is also presented. These results may be used for interpolation or for comparison with other computation tools which may be developed.

## Problem Formulation

### Flow Field Model

The basis for the flowfield analysis is the VSL3DNQ program the authors obtained from NASA/Langley Research Center<sup>6</sup>. This code solves a viscous shock layer approximation to the Navier Stokes equations for flow over axisymmetric bodies, possibly at angle-of-attack. Intended for use with nonequilibrium flows below 9 km/sec, the program included the effects of chemical nonequilibrium using a five species model (N, N<sub>2</sub>, O, O<sub>2</sub>, NO). Complete body solutions are obtained using a global shock shape iteration procedure. In this process an initial shock shape is either assumed or obtained from another analysis method. Using this shape, a new shock shape is calculated through the VSL solution over the body which may be used as input for subsequent calculations. Such "global" iterations are repeated, usually with shock shape relaxation and/or smoothing, until a converged shape is obtained.

Much of the authors' previous work has concentrated upon the solution of the stagnation streamline of spherical nose bodies. This solution is relatively insensitive to the full shock shape, and accurate solutions can be obtained by using an initial shock

\* Visiting Assistant Professor, Member AIAA

\*\* Professor Aerospace Engineering, Associate Fellow AIAA

shape corresponding to another spherical nose body and scaling the stand-off distances to the calculated values. In this paper, the authors have considered the entire nose region of 60 degree sphere cones at zero angle-of-attack. For these cases, global flow solutions up to a surface distance 1.1 times the nose radius were calculated. This distance is well beyond the sphere-cone junction and is a region where the streamwise flow is supersonic everywhere except in the inner surface boundary layer. The latter is necessary to avoid shock shape convergence problems posed by an improper downstream boundary condition.

The original VSL3DNQ code has been extensively modified to extend its nonequilibrium capabilities. The chemistry package has been expanded to include up to 13 reacting species which are specified at run time by the user. Up to 50 chemical reactions may be input by providing both forward and reverse rates, or simply a forward rate with the reverse rate calculated internally via an equilibrium constant. The method of determining the equilibrium constants will be discussed in detail in a following section.

The program now includes thermal nonequilibrium effects through either a 2 temperature,  $T$ - $T_v$ , or 3 temperature,  $T$ - $T_v$ - $T_e$ , model<sup>4</sup>. In the 2 temperature model, the rotational and heavy particle translational energies are assumed to be in equilibrium at the temperature  $T$ , while the vibrational, electronic, and free electron translational energies are assumed to be in equilibrium with each other at the temperature  $T_v$ , which may be different from  $T$ . In the three temperature model, nonequilibrium may exist between the vibrational energy,  $T_v$ , and the electron and electronic energy,  $T_e$ .

For both models, energy exchange between the translational and vibrational modes is modeled using a modified Coupled Vibration-Dissociation-Vibration (CVDV) method<sup>7,8</sup>. The modifications consist of the relaxation time limiting and total rate adjustment suggested by Park<sup>9,10</sup>. Energy is exchanged between free electrons and heavy particles using an elastic collision model, and a free electron energy loss due to electron impact ionization and dissociation is included. For the three temperature model, an additional exchange of energy between electron and vibrational modes is modeled using the rates from J. H. Lee<sup>11</sup>. Also, two forms of the electron energy equation are available: a complete differential equation including all terms and an approximate algebraic equation obtained by dropping all terms but the exchange terms (translational to electron, vibrational to electron, and electron impact depletion). The latter equation is called the quasi-electron-electronic equation and is useful when starting solutions from an assumed initial profile or when low electron concentrations yield numerical difficulties with the differential equation.

The effect of multi-temperatures on chemical reactions rates has also been modeled. For the forward dissociation rates of  $O_2$ ,  $N_2$ , and  $NO$ , the CVDV method includes a rate correction based upon the difference between  $T$  and  $T_v$ . This correction is applied to the forward rate calculated from  $T$  alone. The electron impact reactions forward rates are calculated using the electron temperature,  $T_e$ . For all other reactions the forward rates are calculated based upon the heavy particle translational temperature.

While reverse rates may be input directly, the authors gener-

ally use the reaction equilibrium constants to calculate the reverse rate. This method guarantees an equilibrium species concentration independent of the input rates. The equilibrium constants in turn are calculated from the species partition functions. Currently, the partition functions are obtained assuming fully excited rotational and vibrational modes without coupling between them, and assuming a harmonic oscillator<sup>5</sup>. The partition functions are always calculated using the three characteristic temperatures, thus yielding equilibrium constants which are also functions of all three temperatures.

This method for calculating the equilibrium constant influences the dependence of the reverse reaction rate. For the electron impact reactions, the reverse rates are strong functions of the electron temperature and weak functions of the heavy particle translational and/or vibrational temperature. The reverse rates for the dissociation reactions are obtained from the uncorrected forward rate (i.e. based upon  $T$  only) and the equilibrium constant. The reverse rates are thus strong functions of  $T$  and weaker functions of  $T_v$  and  $T_e$ . For the remaining reactions, the dependency can be complex and each requires an individual study.

Park<sup>12</sup> suggests an alternate method for calculating reverse rates using equilibrium constants and forward rates calculated using appropriate temperatures to obtain the expected reverse rate dependency. An attempt by the authors to use similar methods had the tendency to severely slow down some reactions like dissociation while greatly speeding up others like the ion exchange rates. In particular, in the shock front region where translation temperatures are high, the high rates for ion exchange were driving the chemical model to a quasi-equilibrium well before there was thermal equilibrium. Since the whole concept of using equilibrium constants in strong chemical and thermal nonequilibrium regions is in question, the authors opted for the previously described method which for their analysis yielded more reasonable results and had the expected physical consequence that chemical equilibrium was delayed until thermal equilibrium occurred.

The thermodynamic variables  $c_p$  and  $H$  are calculated using characteristic temperatures of rotation and vibration with the same basic assumptions as for the partition functions. The electronic contribution to both terms are modeled by including up to eight electronic energy levels.

The coefficients of conduction and viscosity are currently calculated using the collision cross section method of Gnoffo et al.<sup>13</sup> and includes multi-temperature effects. A full multicomponent diffusional model was developed<sup>4</sup> as part of this research program, but results obtained using this model are not significantly different from those obtained using a simple constant Lewis number, binary gas diffusion method<sup>14</sup>. Thus, all the results in this paper were obtained using the constant Lewis number model.

### Radiation Model

The radiation method being used has been derived from the RADICAL (or RAD/EQUIL) code of Nicolet<sup>15,16</sup>. The radiation portion of RADICAL performs an equilibrium radiation analysis of a heated gas between a shock front and wall. The method includes the effects of self-absorption and variable wall optical

properties. The radiating gas system includes all the primary radiating species of oxygen, nitrogen, argon, hydrogen and many common carbon molecules which appear around ablating surfaces.

Since the RADICAL code was developed with the goal of performing the radiation analysis efficiently and to good accuracy, the following approximations have been made. First, a tangent slab approximation is used. Under this assumption, the properties of the gas are assumed constant in the surface tangent directions. For blunt bodies where the shock standoff distance is typically on the order of 6 percent of the nose radius or less, this approximation should be valid. Second, to speed up calculation of the absorption function, the program uses line groupings internally for which the underlying continuum absorption may be assumed nearly constant. The frequency width of these line groupings is selectable by the user and have been chosen to reduce the error introduced by this assumption. Third, the molecular radiation contribution, while being a line phenomena, is calculated using a band model approximation. These models have been curve fit to experimental results and generally yield accurate results for the total radiative contribution but lack the detailed information more recent methods yield. However, due to the enormous computational savings obtained with the band model, their use is still desirable for many applications. Lastly, while most of the atomic bound-bound transitions are handled as discrete lines, the transitions between the very upper states of oxygen and nitrogen have been curve fit with band approximations. These transitions occur in the far infrared and do not contribute greatly to the total radiative flux; but again, the band modeling trades off some detailed information for the sake of computational efficiency.

The authors have developed two methods for including atomic local thermodynamic nonequilibrium (LTNE) effects, termed the first and second order models (Refs. 17,14,5). The first order model is based upon the observation by Wilson<sup>18</sup> that the lower three electronic states of nitrogen (and also oxygen) and all the upper states have relatively small energy differences between adjacent states when compared to the energy difference between the third and fourth states. Thus a limiting step in the excitation to ionization of nitrogen and oxygen is the excitation between low lying states to the upper states across the 3-4 energy jump. Wilson used this observation to deduce a electron impact ionization rate for nitrogen which correlated well with the observed experimental ionization rates in nonequilibrium flow. The first order LTNE model extends this concept to a radiation model by adding the assumptions that the lower three states of both nitrogen and oxygen will be in near thermodynamic equilibrium with each other while the upper states will be in near equilibrium with each other and with the ionized state and free electrons. Since the relative populations of the ground state and ionized state are calculated using the chemical rate equation, this assumption ties the existence of thermodynamic equilibrium in nitrogen and oxygen to the formation of chemical equilibrium of the electron impact ionization reaction. These assumptions inhibit a burst of radiation which would otherwise be predicted near the electron temperature peak behind the shock front and yield results in good agreement with flight and shock tube measurements<sup>4,5</sup>.

To test the validity of the assumption of equilibrium between

the upper level states and the ionized states, the second order LTNE method was developed. In this method, thermodynamic equilibrium is still assumed between the low lying states and between the upper states, but excitation rates between the lower and upper levels as well as ionization rates from both the lower and upper levels are calculated using chemical rates deduced from the transition studies of Kunc and Soon<sup>19,20</sup>. The model is implemented by introducing the upper level states of both oxygen and nitrogen as two new species in the thermodynamic and chemical modeling of the flow, and allowing the relative nonequilibrium between all three species (ground, excited, and ionized) to be calculated as part of the flow field. Results from this method<sup>4,5</sup> indicate that while the second order method predicts less upper state deviation from equilibrium than the first order method, the two methods predict total radiation fluxes in close agreement and similar in spectral variance. Since the second order method suffers from being numerically stiff due to the fast chemical rates for ionization of the excited states, the first order method is more suitable for everyday calculations.

As in most equilibrium radiation analysis, the absorption coefficients used by RADICAL are calculated using radiative cross sections which have been evaluated in terms of the total species population density as opposed to the population of the particular states involved. Thus, a Boltzmann electronic state population is explicitly assumed. Also for equilibrium, the radiative source function reduces to simply the black body function. From the true nonequilibrium absorption and source functions<sup>21</sup> it can be shown<sup>5</sup> that the equilibrium values can be corrected for LTNE by factors determined from the ratio of actual state populations to state populations predicted by Boltzmann equilibrium. These LTNE correction factors are easily determined from the flow field solution and applied to the internal radiation calculations of RADICAL. This method of LTNE correction is common to both of the radiative nonequilibrium models described above.

The radiating molecular bands modeled by Nicolet in the RADICAL package include the contributions from  $N_2$ ,  $O_2$ ,  $NO$ , and  $N_2^+$ , with the later two species being the largest radiators. While this research has mainly concentrated upon the development of methods for atomic LTNE, it was desired to have some reasonable means for also estimating the molecular LTNE effects for the above species. A simple model had been developed by Carlson et al.<sup>17</sup> using arguments similar to the first order atomic LTNE model. However, due to the more complex methods of vibrational and electronic excitation in molecules and since most molecules do not show a decisive split in the energy states of ground and excited states this method was subsequently considered to be too approximate. Instead, the quasi-steady state method (QSSM) of Park<sup>9</sup> has been used. The basic assumption of this method is that given the total species number densities of atoms and molecules from a gasdynamic solution, the excited state populations of the molecules can be calculated by balancing the rates of excitation and de-excitation through electron collisions, heavy particle collisions, and spontaneous radiative emissions (radiative absorption is not included). This method typically predicts that the  $N_2^+$  molecule is never far from being in Boltzmann equilib-

rium and thus may overpredict the amount of molecular radiation at lower flight speeds<sup>5</sup>. However, the level of molecular radiation is also very strongly influenced by the chemical dissociation model and the QSSM method suffices until there is more experimental verification of the currently available models.

### Radiation-Gasdynamic Coupling

To account for the loss or gain of energy from the flowfield due to radiative effects, additional terms must be added to the governing energy equations. For the global energy equation, this process is straight forward since it is obvious that any change in the local radiative energy flux must come from some form of gasdynamic energy. The total flux quantity,  $\nabla \dot{q}_r$ , is thus added as a scalar property into the global energy equation.

If all the processes of radiative emission and absorption are considered, it is seen that portions of the total flux are being absorbed or emitted as: chemical energy in the breaking of bonds (photo-ionization and photo-dissociation), electronic energy state transitions, excess ionization energy imparted to freed electrons, free-free electron energy, changes in vibrational energy states, and changes in rotational energy states. These effects are listed in order of magnitude for radiation associated with very high speed reentry such as lunar or Martian return where atomic radiation dominates and radiative-gasdynamic coupling is very important. At lower velocities such as those for the AFE, molecular radiation dominates and the first source (chemical bonding energy) may be much less than the other sources. The magnitude of radiative-gasdynamic coupling is also much less important at the lower velocities. The last two sources potentially affect the vibrational and rotational energy although they are generally not included by investigators.

The fraction of the total energy flux not expended in breaking chemical bonds should be accounted for as a loss or gain of electron-electronic energy. To do this, however, requires a detailed accounting in the radiation transport model of each contributing process and the associated radiative energy flux. Such an effort was made by Stanley and Carlson<sup>22</sup> in their consideration of hypersonic precursor effects. A review of their work shows the great difficulty involved in extracting photo-ionization rates out of the radiation calculation even when only considering a simplified radiative model. The extensive numerical considerations which would have to be made in order to include photo-ionization processes and to properly model the gain or loss of electron-electronic energy are beyond the scope of this work. Further, the total effects of including these phenomena is not considered important at the conditions to be considered but may have some applicability to higher altitude, lower density flows.

### Discussion of Results

Results have been obtained using the above analysis method for a wide range of nonequilibrium flight conditions as shown in Table I. The altitudes selected for analysis were 70, 75, and 80 km for which the corresponding freestream densities are  $8.753\text{E-}5$ ,  $4.335\text{E-}5$ , and  $1.995\text{E-}5 \text{ kg/m}^3$ , respectively. Over this range, the flowfields vary from being predominately in chemical and

Alt. (km)	Rnose (m)	Vel. (km/sec)	$\Delta$ (cm)	$Q_c$ (W/cm <sup>2</sup> )	$Q_r$ (W/cm <sup>2</sup> )
80	2.3	9	13.51	8.75	1.55
80	2.3	10	13.95	16.0	4.12
80	2.3	12	12.31	36.0	27.8
80	2.3	14	10.70	64.1	90.1
80	2.3	16	9.66	97.8	197.
75	2.3	9	12.03	13.5	2.30
75	2.3	10	12.54	24.7	8.83
75	2.3	12	11.17	55.0	83.4
75	2.3	14	9.74	97.3	265.
75	2.3	16	8.73	151.	560.
70	2.3	9	11.27	26.4	3.60
70	2.3	10	11.83	43.0	21.2
70	2.3	12	10.70	88.8	216.
70	2.3	14	9.42	153.	644.
70	2.3	16	8.52	227.	1296.
75	1.0	9	6.09	21.5	1.80
75	1.0	10	6.28	39.3	5.10
75	1.0	12	5.52	85.1	45.1
75	1.0	14	4.82	150.	169.
75	1.0	16	4.34	226.	368.
75	0.5	9	3.46	34.0	1.08
75	0.5	10	3.49	52.6	2.72
75	0.5	12	3.23	128.	25.4
75	0.5	14	2.79	223.	98.0
75	0.5	16	2.54	340.	237.

Table I: Summary of Cases and Stagnation Results

thermal equilibrium to having large regions of nonequilibrium. This variance is shown by the temperature and mole fraction profiles in Figs. 1 and 2 for a flight velocity of 16 km/sec and altitudes of 70 and 80 km, respectively. At 70 km, the profiles indicate that equilibrium exists for approximately 85 percent of the shock layer although a slight gradient in both temperature and species concentration exist due to radiative cooling. By contrast, at 80 km only 65 percent of the shock layer is in equilibrium, and the nonequilibrium region near the shock front has almost tripled in size to one quarter of the standoff distance. The lower altitude represents a practical limit to the applicability of nonequilibrium analysis methods due to the numerical stiffness of most chemical nonequilibrium models. In fact, the solution at 16 km/sec and 70 km without radiative cooling could not be obtained due to numerical oscillations in the equilibrium region. Similarly, the altitude of 80 km may represent a practical limit for the applicability of continuum methods or at least shock fitted methods such as VSL due to the thickening of the shock itself as density decreases further.

The velocities selected for study ranged from 9 to 16 km/sec. The higher speed, 16 km/sec, is near the maximum reentry velocity of missions and configurations currently being considered. As seen in both Figs. 1 and 2, equilibrium ionization is almost 50 percent at this speed and almost no molecular species

exist outside the shock front nonequilibrium layer. The radiative spectra at this speed is correspondingly dominated by atomic radiation processes as shown in Fig. 3. The lower part of this figure shows the actual detailed spectral content of the radiation incident upon the wall. The upper plot makes use of the internal line groupings in RADICAL to combine the total contributions of closely grouped lines and, due to the linear axis, is more indicative of the actual contribution of various spectral regions. Almost all of the radiation from molecules lies in the range of 2-4 eV and is obviously a small contribution to the total at this speed. By contrast, at 9 km/sec the flow is ionized by less than 0.5 percent and the molecular nitrogen population is significant throughout the shock layer as seen in Fig. 4. The corresponding radiative spectra at 9 km/sec (shown in Fig. 5) consists almost solely of molecular radiation. Thus, this speed represents a lower limit for the need of an atomic nonequilibrium radiation model which is the main thrust of the author's work.

All the bodies considered were 60° sphere cones with nose radii ranging between 0.5 and 2.3 m. The upper value corresponds to the well reported AFE configuration while the lower was selected as a reasonable minimum radius for a nonablating surface, although, as the results show, convective heating at most of the higher velocities would probably dictate the use of ablating materials. The flowfield model does not currently have a ablating surface capability, nor have the authors made any attempt to include typical ablation products in the radiation analysis, although the original RADICAL analysis does include many.

All the results which will be shown were calculated assuming a nonablating, radiative black wall surface at a fixed temperature of 1650°K. This temperature is a reasonable maximum temperature for the next generation, reusable, heat shield material. The gas mixture modeled was an eleven component air mixture using the chemical reaction set shown in Table II. The wall is assumed to be noncatalytic with respect to molecular recombinations, but catalytic to ionic recombinations. This is consistent with the properties of reactive cured glass (RCG) type surface materials. The diffusion model used is a constant Lewis model approach which yields results in good agreement with a full multi-component diffusional model developed by the authors as mentioned earlier.

The computational grid included 99 points between the fitted shock and the wall with clustering of grid points to both the shock front and wall thermal boundary layer. Downstream marching was performed using a step of  $\Delta S = 0.1$  of the nose radius and was continued to a value of  $S/R_{\text{nose}} = 1.1$ . Note that the sphere-cone junction occurs at  $S/R_{\text{nose}} = 0.524$  and at the last point, only the inner viscous boundary layer region was subsonic. To avoid numerical difficulties associated with the surface curvature discontinuity at the sphere-cone junction, a joining function was included which smooths the curvature jump out over the adjacent streamwise step locations. The function used is:

$$\kappa = \frac{1}{2} + \frac{1}{\pi} \arctan \left[ \frac{(S_j - S)}{S_j} W \right]$$

The factor  $W$  controls the extent of smoothing; a value of 12 was used in the calculations.

	Reaction	A	B	E
1	$N_2 + M1 = N + N + M1$	$3.00 \times 10^{22}$	-1.6	113200
2	$N_2 + M2 = N + N + M2$	$7.00 \times 10^{21}$	-1.6	113200
3	$O_2 + M1 = O + O + M1$	$1.00 \times 10^{22}$	-1.5	59500
4	$O_2 + M2 = O + O + M2$	$2.00 \times 10^{21}$	-1.5	59500
5	$NO + M3 = N + O + M3$	$1.10 \times 10^{17}$	0.0	75500
6	$NO + M4 = N + O + M4$	$5.00 \times 10^{15}$	0.0	75500
7	$O + e^- = O^+ + e^- + e^-$	$6.35 \times 10^{15}$	0.0	106200
8	$N + e^- = N^+ + e^- + e^-$	$5.08 \times 10^{16}$	0.0	121000
9	$NO + O = N + O_2$	$8.40 \times 10^{12}$	0.0	19450
10	$N_2 + O = NO + N$	$6.40 \times 10^{17}$	-1.0	38400
11	$N_2 + e^- = N + N + e^-$	$3.00 \times 10^{24}$	-1.6	113100
12	$N + O = NO^+ + e^-$	$5.30 \times 10^{12}$	0.0	31900
13	$N + N = N_2^+ + e^-$	$2.00 \times 10^{13}$	0.0	67500
14	$NO^+ + O = N^+ + O_2$	$1.00 \times 10^{12}$	0.5	77200
15	$N^+ + N_2 = N_2^+ + N$	$1.00 \times 10^{12}$	0.5	12200
16	$O^+ + NO = N^+ + O_2$	$1.40 \times 10^5$	1.9	26600
17	$NO^+ + N = O^+ + N_2$	$3.40 \times 10^{13}$	-1.08	12800
18	$O^+ + N_2 = N_2^+ + O$	$9.10 \times 10^{11}$	0.36	22800
19	$NO^+ + N = N_2^+ + O$	$7.20 \times 10^{13}$	0.0	35500
20	$O + O = O_2^+ + e^-$	$1.10 \times 10^{13}$	0.0	80600
21	$O_2^+ + N = N^+ + O_2$	$8.70 \times 10^{13}$	0.14	28600
22	$O_2^+ + N_2 = N_2^+ + O_2$	$9.90 \times 10^{12}$	0.0	40700
23	$O_2^+ + O = O^+ + O_2$	$4.00 \times 10^{12}$	-0.09	18000
24	$NO^+ + O_2 = O_2^+ + NO$	$2.30 \times 10^{13}$	0.41	32600
25	$NO^+ + O = O_2^+ + N$	$7.20 \times 10^{12}$	0.29	48600
26	$N + M5 = N^+ + e^- + M5$	$2.34 \times 10^{11}$	0.5	120000

Rates in the form  $k_f = A T^B \exp(-E/T)$ .

$T = T_e$  in electron impact reactions:

$M1 = N, N^+, O, O^+$

$M2 = N_2, N_2^+, O_2, O_2^+, NO, NO^+$

$M3 = N, N^+, O, O^+, NO$

$M4 = N_2, N_2^+, O_2, O_2^+, NO^+$

$M5 = N, N^+$

Table II: Reaction System for Air

### Stagnation Point Results

The stagnation point solutions for shock standoff distance, convective heat flux and radiative heat flux to the wall are included in Table I and shown graphically in Figs. 6-8. Results obtained by Sutton and Hartung<sup>23</sup> for equilibrium radiatively coupled shock layers are presented in Table III for comparison. The equilibrium results were linearly interpolated by density from the altitudes considered in Ref. 23. The stagnation standoff distances (Fig. 6) show a local maximum near 10 km/sec as has been seen in the equilibrium results. This maximum roughly divides the flight regimes for which molecular dissociation dominates the flow field (below 10 km/sec) from that for which ionization processes dominate (above 10 km/sec). The standoff distances themselves compare well with the equilibrium results but are consistently higher as would be expected. The smallest difference is approximately 10 percent for the lowest altitude and largest nose radius. The difference increases with both increasing altitude and decreasing nose radius due to the larger extents of nonequilibrium in the shock layer with both changes.

Alt. (km)	Rnose (m)	Vel. (km/sec)	$\Delta$ (cm)	$Q_r$ (W/cm <sup>2</sup> )
80	2.3	9	9.74	0.11
80	2.3	10	10.24	3.71
80	2.3	12	9.39	36.0
80	2.3	14	8.56	110.
80	2.3	16	7.93	242.
75	2.3	9	9.90	0.43
75	2.3	10	10.45	11.45
75	2.3	12	9.53	106.
75	2.3	14	8.59	314.
75	2.3	16	7.83	649.
70	2.3	9	10.08	1.37
70	2.3	10	10.65	28.7
70	2.3	12	9.67	258.
70	2.3	14	8.61	734.
70	2.3	16	7.75	1454.
75	1.0	9	4.30	0.20
75	1.0	10	4.56	6.86
75	1.0	12	4.23	71.8
75	1.0	14	3.88	227.
75	1.0	16	3.63	489.
75	0.5	9	2.15	0.11
75	0.5	10	2.29	4.30
75	0.5	12	2.14	49.0
75	0.5	14	1.99	162.
75	0.5	16	1.89	358.

Table III: Equilibrium Results from Ref. 23

It is of note that while the shock standoff distance is proportional to nose radius in equilibrium flows, the current nonequilibrium results do not show this simple dependency. At 75 km/sec altitude, a good approximation to the relation between  $\Delta$  and  $R_{nose}$  at a constant velocity is given by:

$$\left(\frac{\Delta_1}{\Delta_2}\right) = 0.87 \left(\frac{R_{nose1}}{R_{nose2}}\right)$$

However, insufficient data was generated to determine if this relationship is valid for a wider range of nose radii or how this functionality varies with freestream density.

In Fig. 7 the calculated conductive heat transfer to the wall at the stagnation point are presented. The convective heat transfer shown is the sum of the heat fluxes due to conduction and due to catalysis of the ionic species at the surface. As expected, as density or velocity are increased, total energy flux in the shock layer increases and the wall heating rate rises, although not in direct proportion. Also, as the nose radius of the body is decreased, the convective heat rate increases due to the thinning of the thermal and viscous boundary layers on the body.

An attempt was made to curve fit the entire convective heat transfer results as a single power function of density, velocity and nose radius using a least squares technique. Examination of the curve fit results showed that a better fit for the upper velocities could be obtained by leaving the 9 km/sec data out of the process.

The variation of heating with velocity apparently experiences a functional change at around the 9 - 10 km/sec range, much like what was seen for the standoff distance. This change could be due to the additional effect of ionic catalytic heating which accompanies significant ionization of the shock layer flow, i.e. above 10 km/sec. The final suggested fit is:

$$Q_c = 115.3 \rho^{0.553} V^{2.36} R_{nose}^{-0.540} (1 - h_w/h_\infty)$$

The calculated convective heating values are shown reduced by this function in Fig. 9. The curve fit is seen to reproduce the original data to within 6 percent at all speeds, and within 3 percent for the velocities above 10 km/sec.

The calculated stagnation point radiative heat fluxes to the body surface are shown in Fig. 8. As with convective heating, the radiative heating is seen to increase with both increasing density and velocity. The reasons for increase are more complex, however, and are closely tied to the equilibrium temperature, density, and composition of the gas mixture behind the shock front. Also, since the total radiative flux depends upon the thickness of the radiating gas layer, the wall radiative flux decreases with decreasing nose radius since the shock standoff distances also decrease. Because of the complex dependency of the factors influencing the radiative heating, all attempts to curve fit the calculated results with simple functions of density, velocity and nose radius resulted in approximations with unacceptable errors.

The comparison of nonequilibrium and equilibrium radiative heating rates in Tables I and III shows that the nonequilibrium results are mostly below that predicted by equilibrium. This would not be the case if the atomic LTNE corrections were not being used to reduce the radiation from the thermal nonequilibrium region where the electron temperature reaches its maximum. The exceptions to this trend are all the 9 km/sec cases and the 10 km/sec case at 80 km; these are the cases which are most dominated by molecular radiation. The conclusion from this is that the current method does predict an added molecular radiative contribution from the thermal nonequilibrium regions. However, a conclusion reached in Ref. 5 from the comparison of predicted to measured Fire 2<sup>24</sup> results was that the current QSSM method for molecular LTNE prediction may in fact be over estimating the amount of molecular species equilibrium and thus the amount of molecular nonequilibrium radiation. Thus, the enhanced nonequilibrium radiation at lower speeds may be in error.

It is of interest to note the impact of radiative cooling on the results. To show this, the radiative heating data in Table I which were obtained with radiative cooling are plotted against the similar results without radiative cooling in Fig. 10. The dashed line in this figure has a slope of one. Thus, all the data points would lie on this line if radiative cooling did not affect the solution. The gradual departure of the data from this line indicates the increasing impact of radiative cooling on the final results. Table IV provides a tabulation of the radiatively uncoupled results for stagnation standoff distance, convective heating and radiative heating. The last column of this table are equilibrium data obtained by linear interpolation by freestream density of the results in Ref. 23. In

Alt. (km)	R <sub>nose</sub> (m)	Vel. (km/sec)	$\Delta$ (cm)	Q <sub>c</sub> (W/cm <sup>2</sup> )	Q <sub>r</sub> (W/cm <sup>2</sup> )
80	2.3	9	13.59	8.79	1.53
80	2.3	10	14.15	17.5	4.75
80	2.3	12	12.66	41.7	31.4
80	2.3	14	11.33	76.8	114.
80	2.3	16	10.68	118.	275.
75	2.3	9	12.14	14.0	2.56
75	2.3	10	12.72	27.4	11.2
75	2.3	12	11.79	65.4	114.
75	2.3	14	10.76	123.	405.
75	2.3	16	10.38	185.	1008.
70	2.3	9	11.32	26.2	3.41
70	2.3	10	12.00	45.5	27.2
70	2.3	12	11.32	98.8	319.
70	2.3	14	10.82	171.	1165.
70	2.3	16	—	—	—
75	1.0	9	6.08	21.0	1.64
75	1.0	10	6.26	38.6	4.69
75	1.0	12	5.57	93.4	50.9
75	1.0	14	5.13	175.	217.
75	1.0	16	4.81	267.	514.
75	0.5	9	3.47	34.0	1.03
75	0.5	10	3.53	53.3	2.77
75	0.5	12	3.29	137.	26.8
75	0.5	14	2.83	245.	112.
75	0.5	16	2.68	387.	291.

Table IV: Summary of Radiatively Uncoupled Results

general, the effect of radiative cooling is to reduce all three of these variables. The results in Table IV were not converged to the same shock shape criteria as the radiative coupled data and thus there appear to be some discrepancies between Tables I and IV; in particular, some of the lower speed cases falsely indicate that the standoff distance and/or the heating rates increased with the addition of radiative cooling.

#### Nose Region Solutions

The variations of shock standoff distance, convective heat flux and radiative heat flux with distance along the body are shown in Figs. 11 through 13. The data in this figures have been nondimensionalized by the values at the stagnation point for each case in order to reduce all the data to a comparable scale. The data have also been grouped by flight velocity which provides the best comparison of related data. From the plots of shock standoff distance it is seen that the shock shape in the nose region is relatively unaffected by nose radius or altitude effects while a variation with velocity is noticeable, but not dramatic. Interestingly, the greatest relative rate of growth of the standoff distance occurs for the 12 km/sec cases. Since the component of velocity normal to the conical body at 12 km/sec is 10.39 km/sec, the maximum growth at this speed may be related to the

maximum in stagnation point standoff distance which was seen to occur near 10 km/sec. Also, the greatest scatter in data occurs for the 10 km/sec cases, but the reason for this behaviour is unclear. This scatter does however have an impact on the radiative heat fluxes as will be seen below.

With the exception of the 9 km/sec cases, the convective heating data shown in Figs. 12 all reduce to a narrow distribution range, although there is a slight trend for the smallest nose radius results to show a greater value in the aft regions. This trend is probably due to the merging of the shock front nonequilibrium layer with the thermal boundary layer as the standoff distance decreases. The data for the 9 km/sec are all noticeably higher in the aft regions than that seen for the other velocities. This higher relative heating may be due to either a lack of significant catalytic heating or to a constant merging of the shock and thermal layers at this speed. The oscillations in the profiles around  $S/R_{\text{nose}} = 0.6$  in all cases is due to both the smoothing of the surface curvature near the sphere-cone junction and numerical problems with the solution when the curvature varies too greatly.

Finally, the downstream variations of radiative flux are shown in Fig. 13. Forward of the sphere-cone junction, the trends for each velocity are relatively constant but the amount of radiation decrease between the stagnation point and juncture decreases with increasing velocity. A noticeable exception to this is the highest radiation flux case (16 km/sec at 70 km) which has a trend significantly different from the other cases at the same velocity. The altered variation for this condition is most likely due to the large amount of radiation cooling which also occurs. Aft of the junction, the radiation flux increases in almost all the cases due to the growth of the shock standoff distance and thus the thickness of the heated gas layer. Also, in the aft region a much larger difference exists between the data for each velocity. Here, the general trend is for the relative amount of aft radiation to be higher for lower densities and smaller nose radii. The greatest difference between cases is seen for the 10 km/sec case which as noted above also had the greatest difference in shock standoff distance variations. As may be expected, the thicker shock layers correspond to the higher heat fluxes, but why this wide difference occurs at this velocity is unknown.

#### Conclusion

An analysis method which includes such phenomena as viscous effects, chemical nonequilibrium, thermal nonequilibrium, thermodynamic nonequilibrium and radiation-gasdynamic coupling has been developed for the analysis of flow over re-entry and aeroassisted flight vehicles. This analysis method has been used to generate results over the nose region of a 60° sphere-cone body at a number of nonequilibrium flight conditions. Comparison of these results with other equilibrium analysis indicates that the net effect of nonequilibrium and in particular atomic LTNE in the shock layer is to reduce the total radiative heat load to the vehicle surface. There is an indication that at low speeds molecular LTNE may enhance the nonequilibrium radiation, but these results are currently in question.

#### Acknowledgement

This work was primarily supported by NASA Grant NAG-1-

1003 from the Langley Research Center, with Dr. Lin C. Hartung as technical monitor.

### References

- <sup>1</sup> Carlson, L. A. and Gally, T. A., "Effect of Electron Temperature and Impact Ionization on Martian Return AOTV Flowfields," *Journal of Thermophysics and Heat Transfer*, vol. 5, No. 1, January 1991, pp. 9-20.
- <sup>2</sup> Carlson, L. A. and Gally, T. A., "Nonequilibrium Chemical and Radiation Coupling, Part I: Theory and Models," *Journal of Thermophysics and Heat Transfer*, vol. 6, No. 3, July-September 1992, pp. 385-391.
- <sup>3</sup> Carlson, L. A. and Gally, T. A., "Nonequilibrium Chemical and Radiation Coupling, Part II: Results for AOTV Flowfields," *Journal of Thermophysics and Heat Transfer*, vol. 6, No. 3, July-September 1992, pp. 392-399.
- <sup>4</sup> Gally, T. A., Carlson, L. A. and Green, D., "A Flowfield Coupled Excitation and Radiation Model for Nonequilibrium Reacting Flows," *Journal of Thermophysics and Heat Transfer*, vol. 7, No. 2, April 1993, pp. 285-293.
- <sup>5</sup> Gally, T. A. and Carlson, L. A., "An Approximate Local Thermodynamic Nonequilibrium Radiation Model for Air," AIAA Paper 92-2972, July 1992.
- <sup>6</sup> Thompson, R. A., "Comparison of Nonequilibrium Viscous Shock Layer Solutions with Windward Surface Shuttle Heating Data," AIAA Paper 87-1473, June 1987.
- <sup>7</sup> Treanor, C. E. and Marrone, P. V., "Effect of Dissociation on the Rate of Vibration Relaxation," *Physics of Fluids*, vol. 5, No. 9, September 1962, pp. 1022-1026.
- <sup>8</sup> Marrone, P. V., "Inviscid, Nonequilibrium Flow behind Bow and Normal Shock Waves, Part I. - General Analysis and Numerical Examples," Cornell Aeronautical Laboratory Report No. QM-1626-a-12(I), May 1963.
- <sup>9</sup> Park, C., "Calculation of Nonequilibrium Radiation in the Flight Regimes of Aeroassisted Orbital Transfer Vehicles," in *Thermal Design of Aeroassisted Orbital Transfer Vehicles*, Progress in Astronautics and Aeronautics, Vol. 96, Ed. H. F. Nelson, AIAA, 1985, pp. 395-418.
- <sup>10</sup> Park, C., "Assessment of Two Temperature Kinetic Model for Ionizing Air," AIAA Paper No. 87-1574, June 1987.
- <sup>11</sup> Lee, J. H., "Electron-Impact Vibrational Excitation Rates in the Flowfield of Aeroassisted Orbital Transfer Vehicles," in *Thermophysical Aspects of Re-entry Flows*, Progress in Astronautics and Aeronautics, Vol. 103, Eds. J. N. Moss and C. D. Scott, AIAA, 1986, pp. 197-224.
- <sup>12</sup> Park, C., Howe, J. T., Jaffe, R. L., and Candler, G. V., "Chemical-Kinetic Problems of Future NASA Missions," AIAA Paper 91-0464, January 1991.
- <sup>13</sup> Gnoffo, P. A., Gupta, R. N., and Shinn, J. L., "Conservation Equations and Physical Models for Hypersonic Air Flows in Thermal and Chemical Nonequilibrium," NASA TP 2867, February 1987.
- <sup>14</sup> Miner, E. W. and Lewis, C. H., "Hypersonic Ionizing Air Viscous Shock Layer Flows over Nonanalytic Blunt Bodies," NASA CR-2550, May 1975.
- <sup>15</sup> Nicolet, W. E., "Advanced Methods for Calculating Radiation Transport in Ablation-Product Contaminated Boundary Layers," NASA CR 1656, September 1970.
- <sup>16</sup> Nicolet, W. E., "Rapid Methods for Calculating Radiation Transport in the Entry Environment," NASA CR 2528, April 1975.
- <sup>17</sup> Carlson, L. A., Bobskill, G. J., and Greendyke, R. B., "Comparison of Vibration Dissociation and Radiative Transfer Models for AOTV/AFE Flowfields," *J. of Thermophysics and Heat Transfer*, vol. 4, No. 1, January 1990, pp. 16-26.
- <sup>18</sup> Wilson, J., "Ionization Rate of Air Behind High Speed Shock Waves," *The Physics of Fluids*, vol. 9, No. 10, October 1966, pp. 1913-1921.
- <sup>19</sup> Kunc, J. A. and Soon, W. H., "Collisional Radiative Nonequilibrium in Partially Ionized Atomic Nitrogen," *Physical Review A*, vol. 40, No. 10, November 15, 1989, pp. 5822 ff.
- <sup>20</sup> Kunc, J. A. and Soon, W. H., "Thermal Nonequilibrium in Partially Ionized Atomic Oxygen," *Physical Review A*, vol. 41, No. 2, January 15, 1990, pp. 825 ff.
- <sup>21</sup> Chapin, C. E., "Nonequilibrium Radiation and Ionization in Shock Waves," AA&ES Report, June 1967, Purdue, Univ., Lafayette, Ind.
- <sup>22</sup> Stanley, S. and Carlson, L. A., "The Effects of Shock Wave Precursors Ahead of Hypersonic Entry Vehicles," AIAA Paper 91-1465, June 1991.
- <sup>23</sup> Sutton, K. and Hartung, L. C., "Equilibrium Radiative Heating Tables for Earth Entry," NASA TM 102652, May 1990.
- <sup>24</sup> Cauchon, D. L., McKee, C. W., and Cornette, E. S., "Spectral Measurements of Gas-Cap Radiation During Project Fire Flight Experiments at Reentry Velocities Near 11.4 Kilometers per Second," NASA TM X-1389, October 1967.

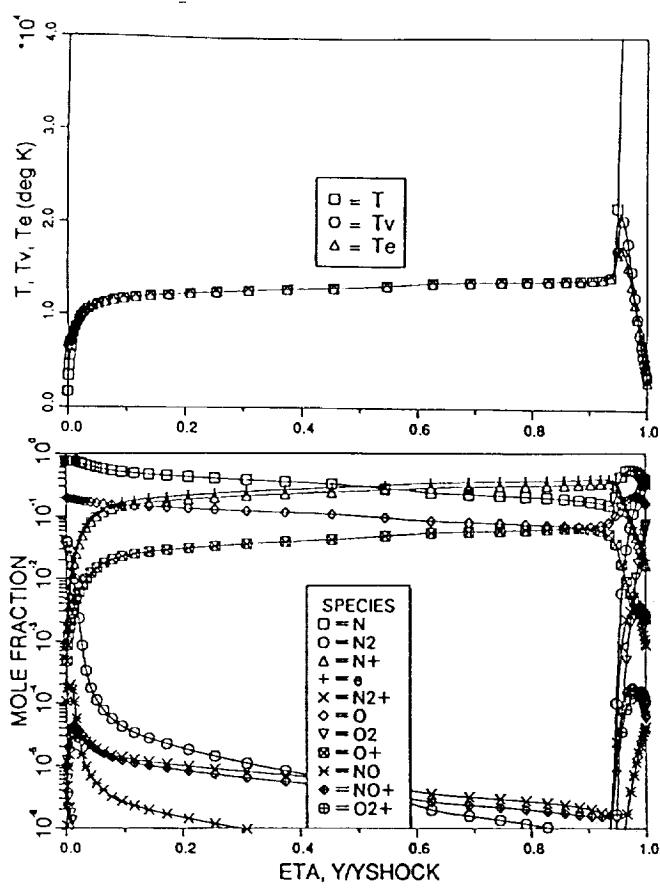


Figure 1: Stagnation Temperature and Mole Fraction Profile  
 $R_{nose} = 2.3$  m,  $V = 16$  km/sec,  $H = 70$  km

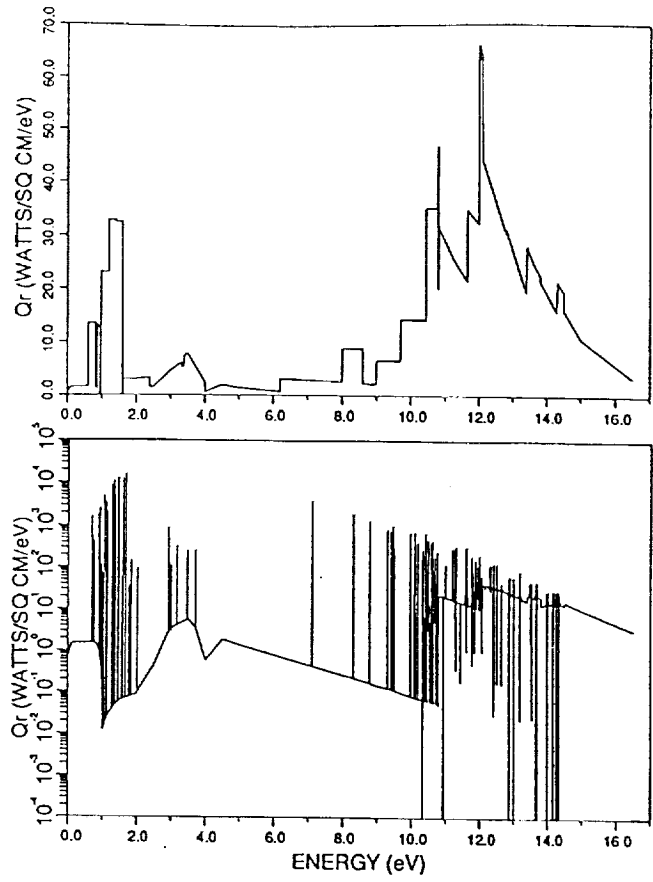


Figure 3: Radiative Heat Flux, Grouped and Detailed Spectra  
 $R_{nose} = 2.3$  m,  $V = 16$  km/sec,  $H = 80$  km

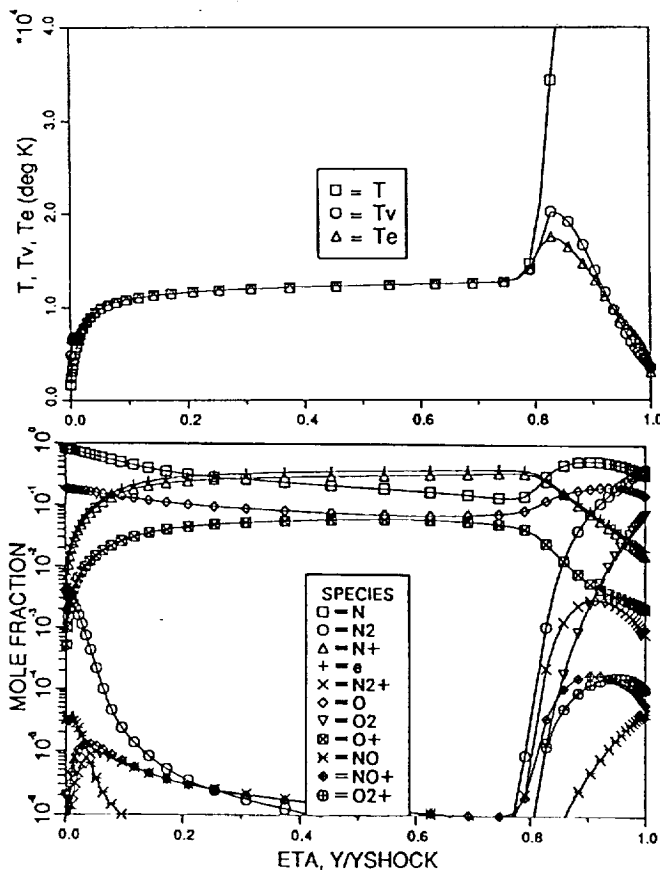


Figure 2: Stagnation Temperature and Mole Fraction Profile  
 $R_{nose} = 2.3$  m,  $V = 16$  km/sec,  $H = 80$  km

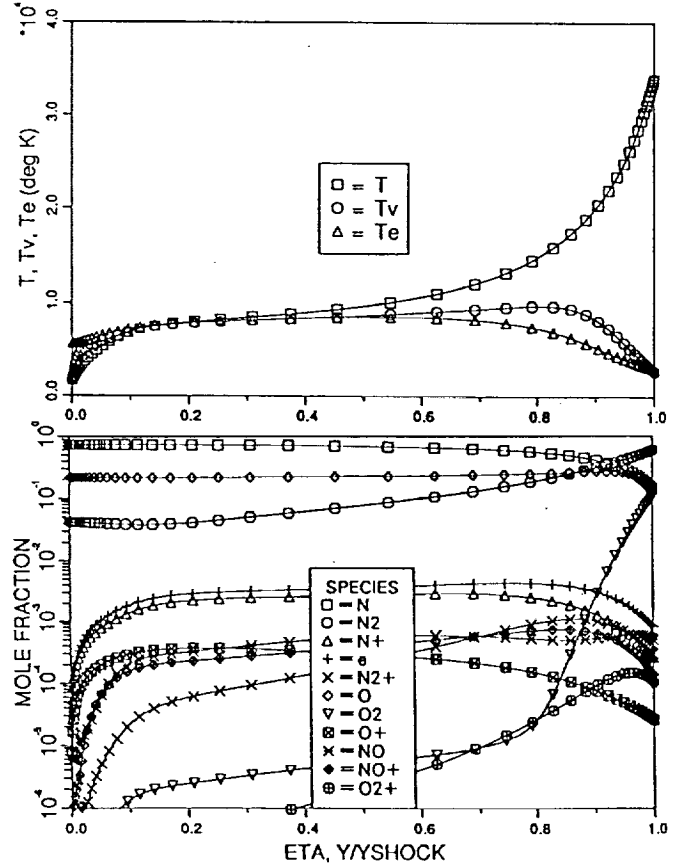


Figure 4: Stagnation Temperature and Mole Fraction Profile  
 $R_{nose} = 2.3$  m,  $V = 9$  km/sec,  $H = 80$  km

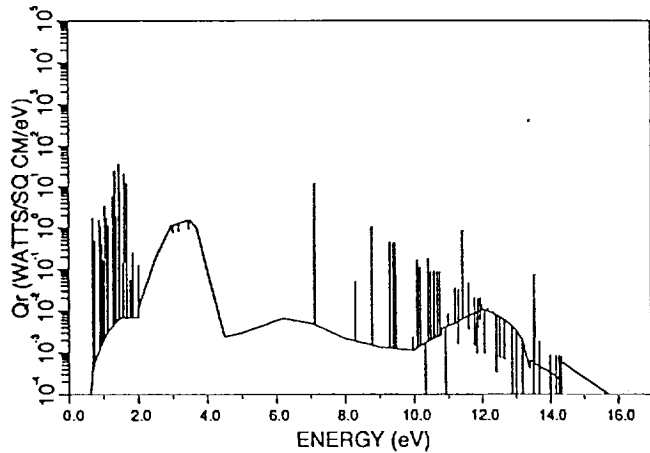
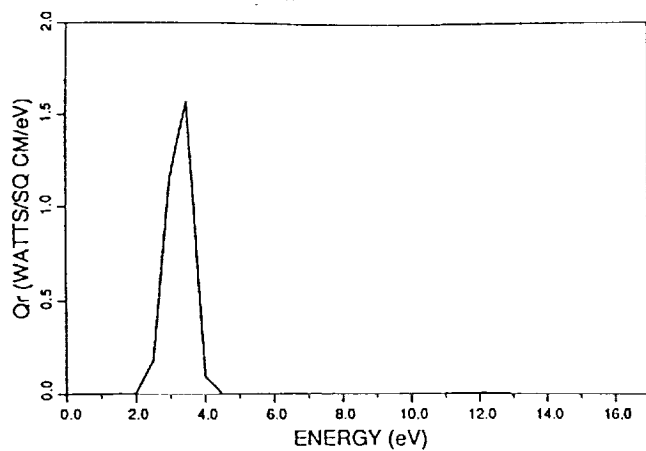


Figure 5: Radiative Heat Flux, Grouped and Detailed Spectra  
 $R_{\text{nose}} = 2.3 \text{ m}$ ,  $V = 9 \text{ km/sec}$ ,  $H = 80 \text{ km}$

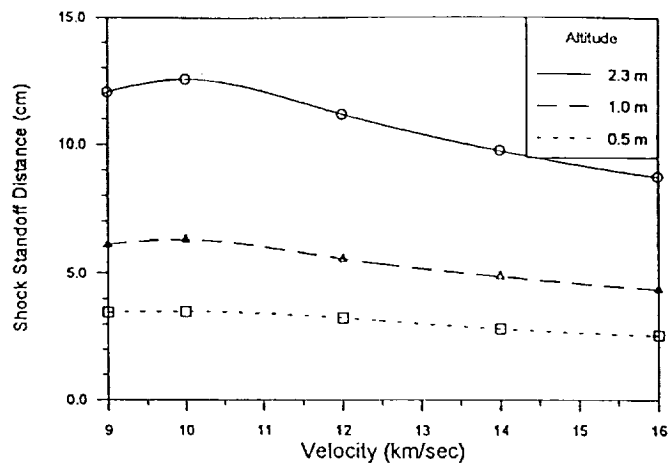


Figure 6: (b) versus nose radius

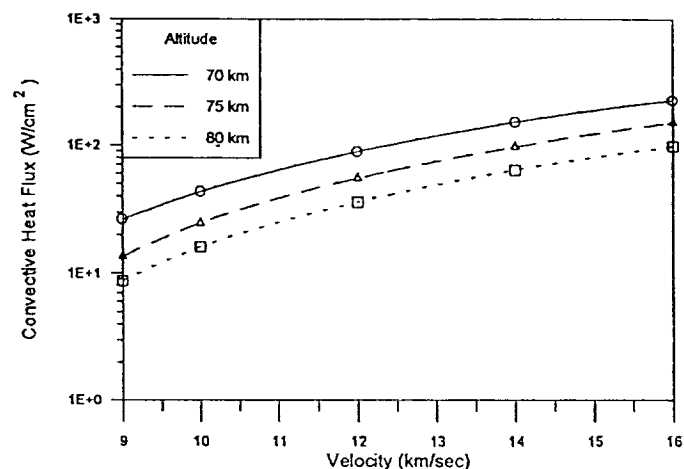


Figure 7: Stagnation Convective Heating Rates  
 (a) versus altitude

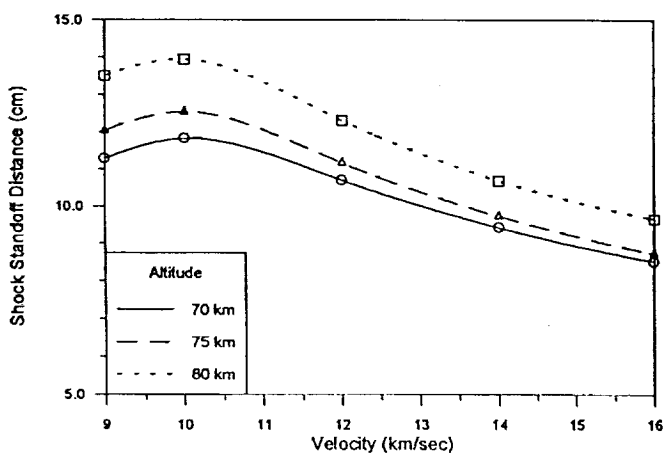


Figure 6: Stagnation Shock Standoff Distances  
 (a) versus altitude

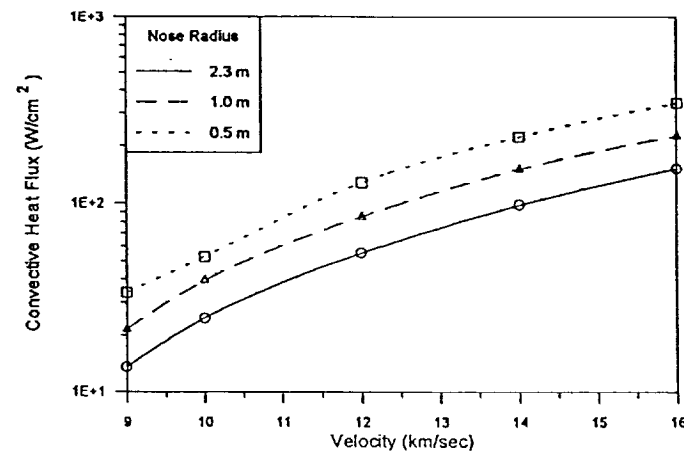


Figure 7: (b) versus nose radius

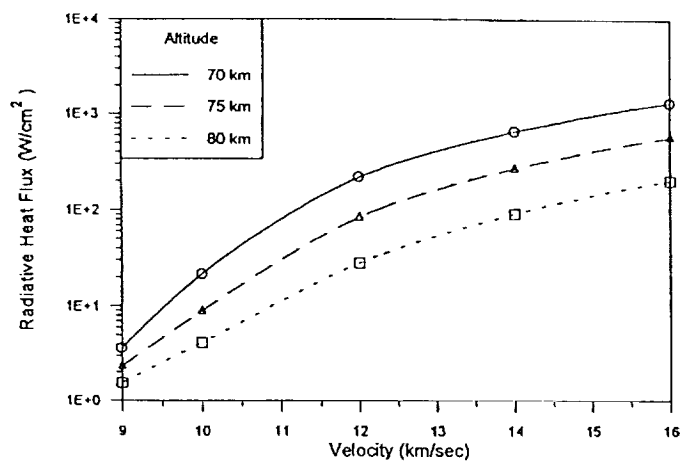


Figure 8: Stagnation Radiative Heating Rates  
(a) versus altitude

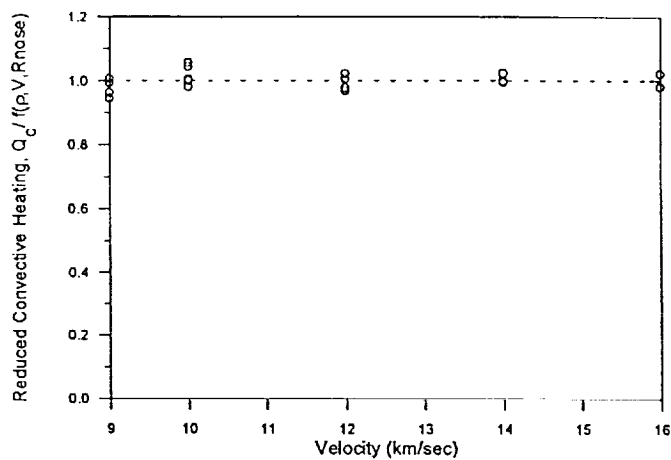


Figure 9: Convective Heat Transfer Correlation

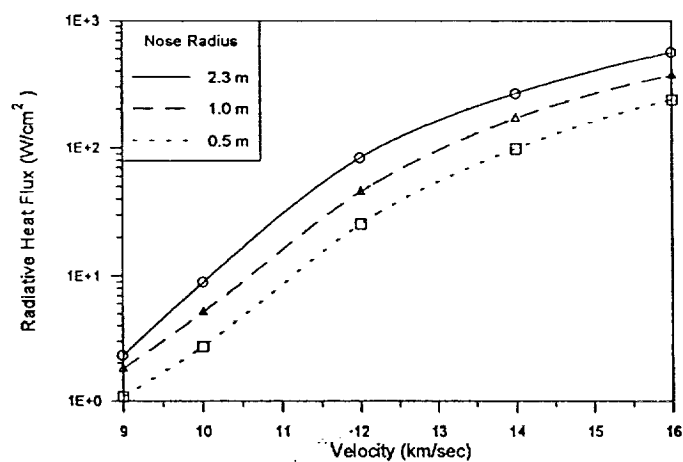


Figure 8: (b) versus nose radius

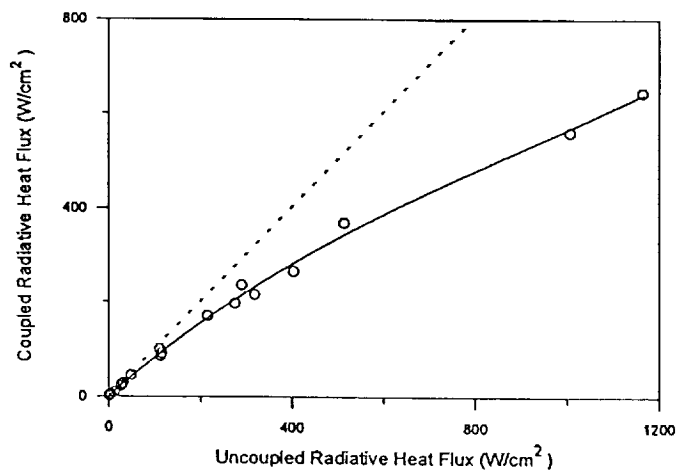


Figure 10: Radiative Cooling Effect of Heat Transfer

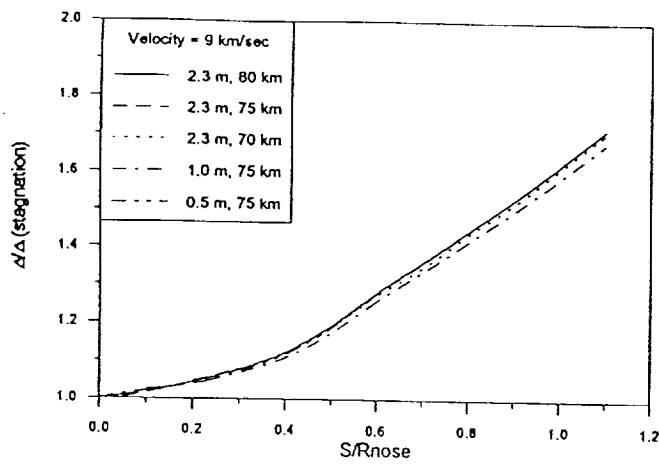


Figure 11: Streamwise Shock Standoff Distance Variations  
(a)  $V = 9$  km/sec

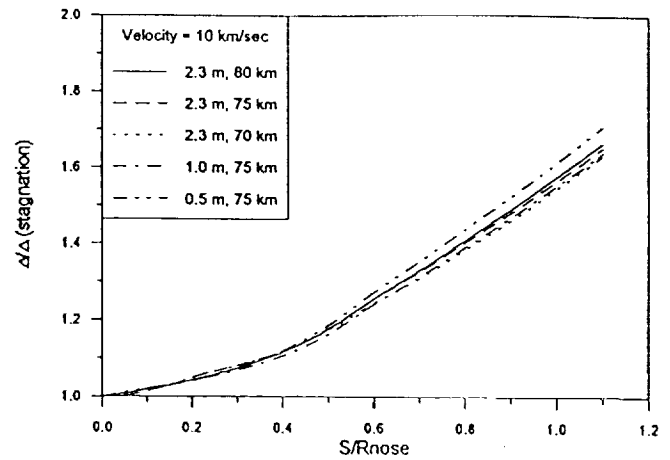


Figure 11: (b)  $V = 10$  km/sec

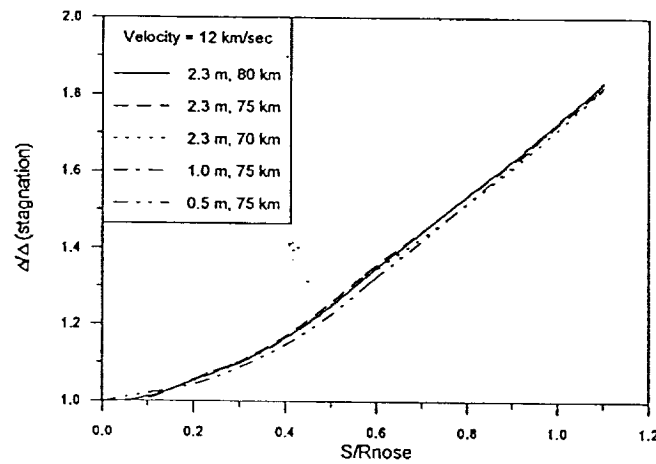


Figure 11: (c)  $V = 12$  km/sec

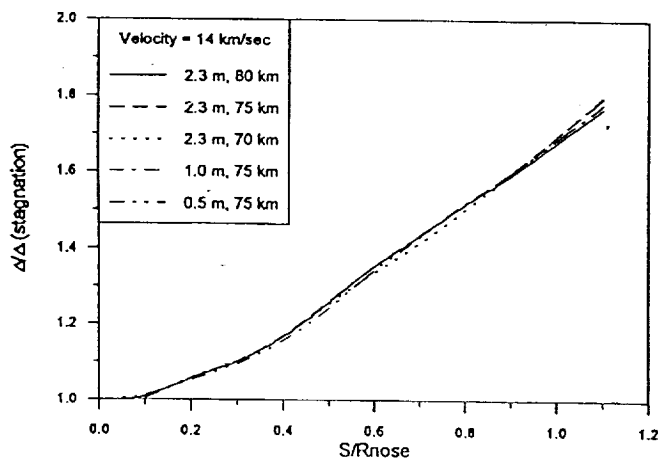


Figure 11: (d)  $V = 14$  km/sec

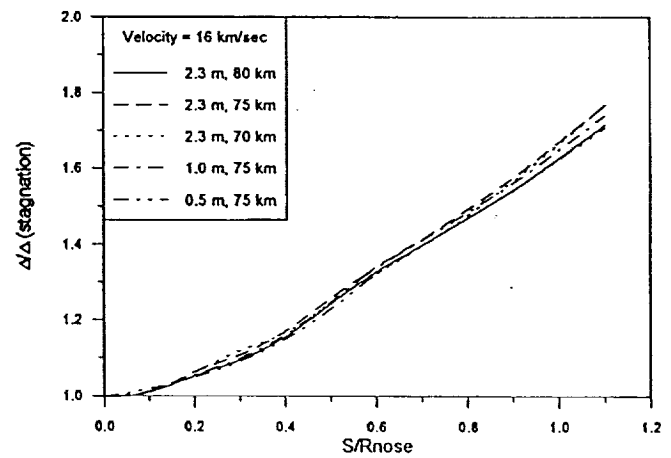


Figure 11: (e)  $V = 16$  km/sec

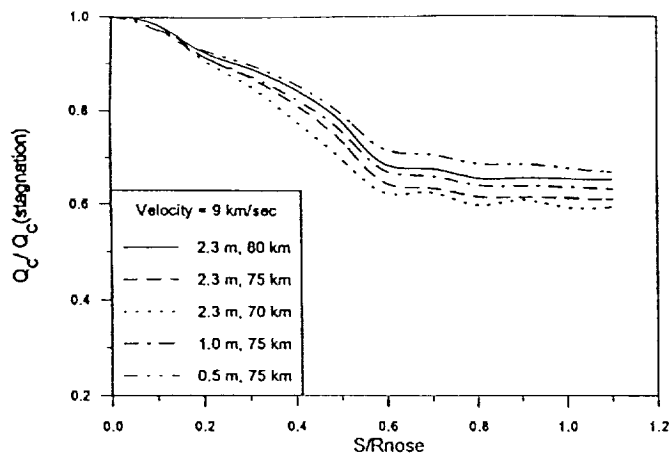


Figure 12: Streamwise Convective Heat Flux Variations  
(a)  $V = 9$  km/sec

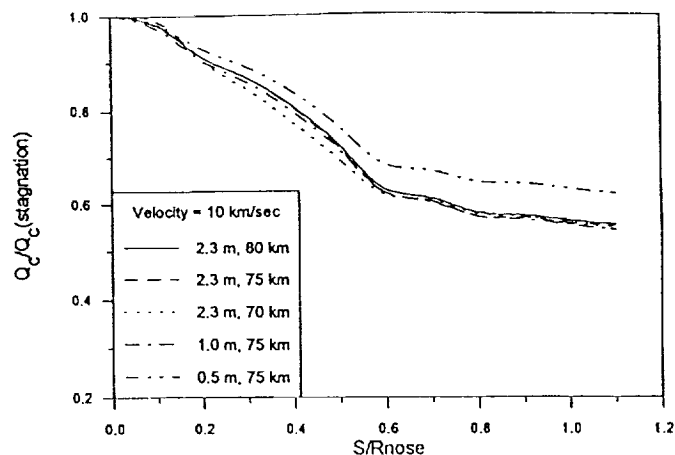


Figure 12: (b)  $V = 10$  km/sec

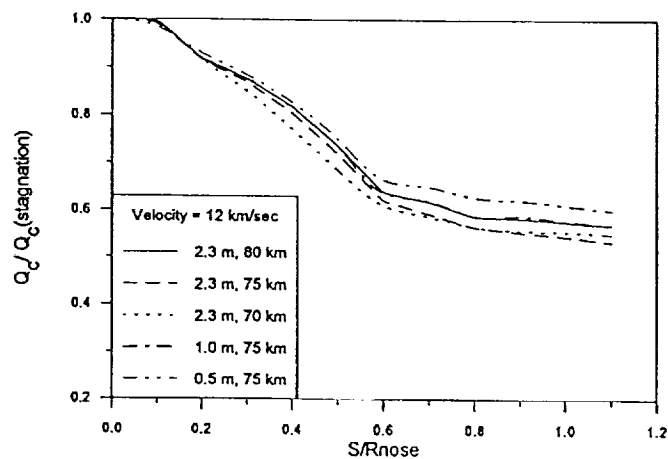


Figure 12: (c)  $V = 12$  km/sec

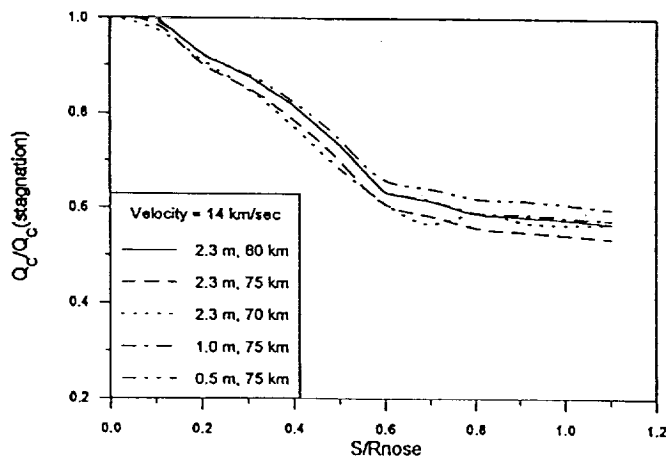


Figure 12: (d)  $V = 14$  km/sec

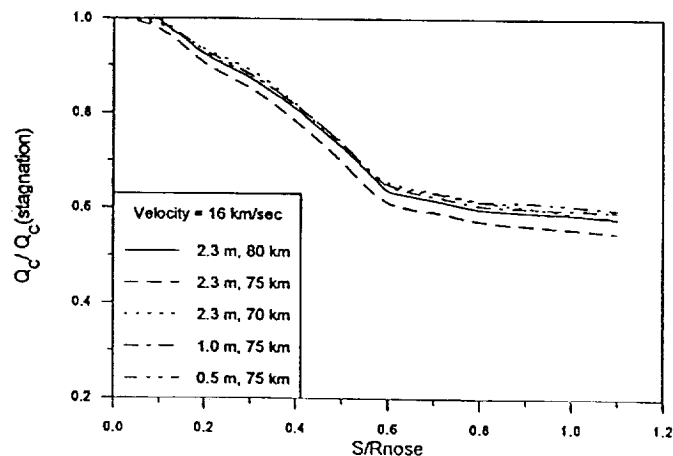


Figure 12: (e)  $V = 16$  km/sec

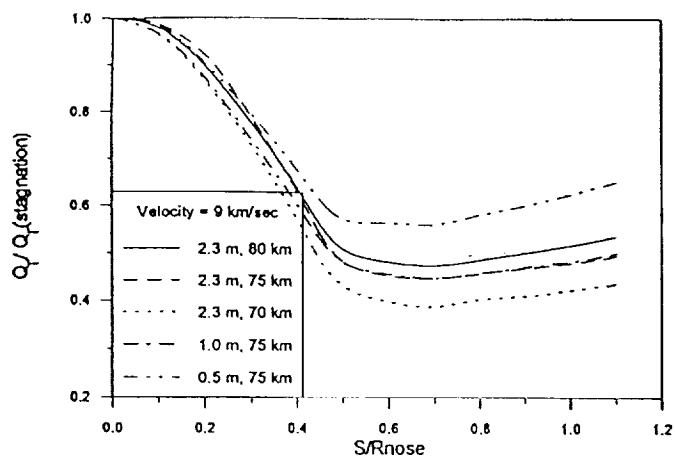


Figure 13: Streamwise Radiative Heat Flux Variations

(a)  $V = 9$  km/sec

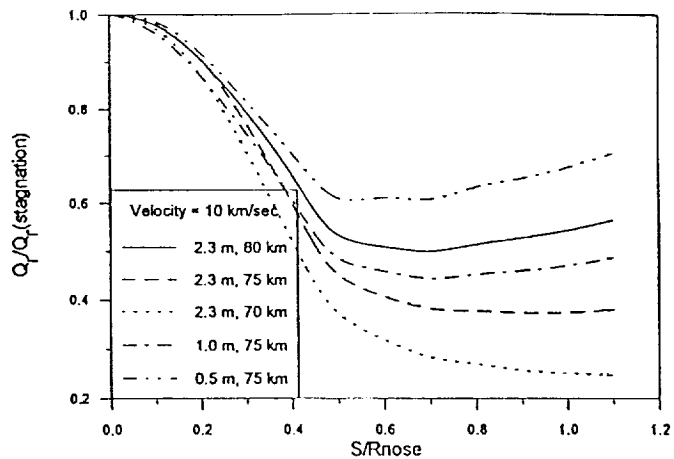


Figure 13: (b)  $V = 10$  km/sec

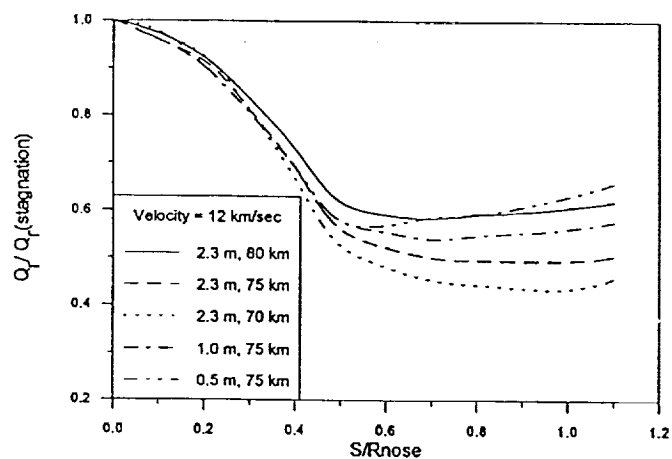


Figure 13: (c)  $V = 12$  km/sec

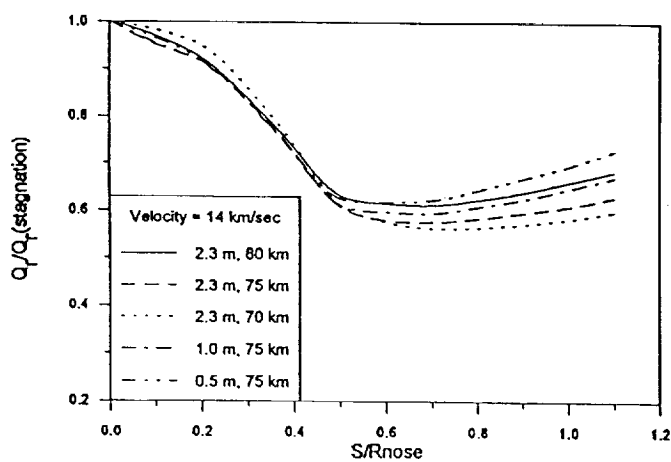


Figure 13: (d)  $V = 14$  km/sec

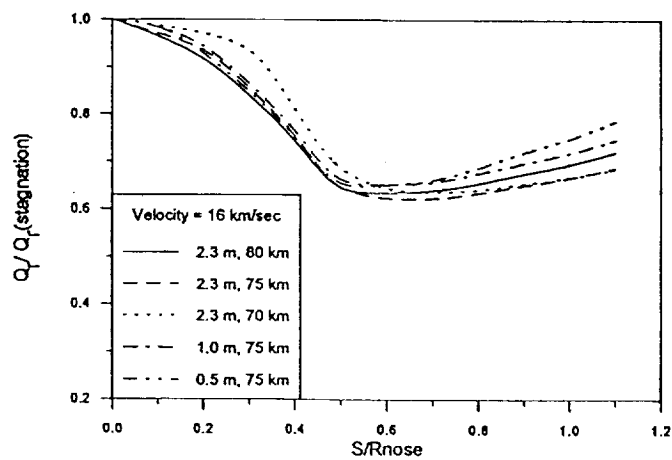


Figure 13: (e)  $V = 16$  km/sec

**Appendix II**

**A Preferential Vibration Dissociation Coupling Model for Nonequilibrium  
Flowfields**

**AIAA Paper 93-3197**

**by**

**David E. McGough  
Leland A. Carlson  
and  
Thomas A. Gally**

# A Preferential Vibration Dissociation Coupling Model for Nonequilibrium Flowfields

David E. McGough\*, Leland A. Carlson\*\*

and

Thomas A. Gally\*\*\*  
Texas A&M University

## Abstract

A preferential vibration-dissociation coupling model is incorporated into a radiatively coupled viscous shock layer code that also includes chemical, radiative, and thermal nonequilibrium. Stagnation point flow profiles are obtained for various Fire 2 flight conditions and for a typical 14 km/sec AOTV case, and comparisons are made with Fire 2 experimental data. Adjustments in molecular absorption coefficients are also made for several diatomic species. Based on comparisons with experimental data, very little preferential dissociation behavior is present in the Fire 2 flight conditions.

## Nomenclature

$c_p$  = constant pressure specific heat  
 $D$  = dissociation energy  
 $e$  = energy per unit mass  
 $E_s$  = energy removed per dissociation  
 $G_s$  = energy gained per recombination  
 $h$  = enthalpy per unit mass  
 $k$  = Boltzmann constant  
 $k_f$  = forward reaction rate constant  
 $k_{eq}$  = equilibrium rate constant  
 $m$  = particle mass  
 $N$  = cut off level in simple harmonic oscillator  
 $N_e, N_i$  = number density  
 $p$  = pressure  
 $Q$  = vibrational partition function  
 $Q_c$  = convective heat transfer  
 $Q_r$  = radiative heat transfer  
 $T$  = temperature

$u^i$  = mass averaged velocity components  
 $U_s$  = diffusion velocity  
 $U$  = preferential temperature  
 $x^i$  = coordinate axis  
 $\eta$  = heat conduction coefficient  
 $\theta_v$  = characteristic vibrational temperature  
 $\rho$  = density  
 $\sigma$  = radiative cross section  
 $\tau$  = relaxation time

## subscripts

$e$  = electronic  
 $f$  = forward rate (production)  
 $r$  = reverse rate (depletion)  
 $s$  = species  
 $sh$  = value at shock  
 $tr$  = translational  
 $v$  = vibrational

## Introduction

Chemical and radiative nonequilibrium effects dominate the flow around many hypersonic vehicles, such as those proposed for aerobraking maneuvers. In previous work<sup>1-4</sup>, a radiatively coupled viscous shock layer (VSL) flow solver was developed from the VSL3DNQ program from NASA Langley<sup>5</sup> and the RADICAL radiation transport method of Nicolet.<sup>6,7</sup> This program currently includes viscous effects, diffusion, conduction, chemical nonequilibrium, and thermal nonequilibrium. The program also includes a method to account for local thermodynamic nonequilibrium (LTNE) effects on radiation emission and absorption.

The coupling between the processes of dissociation and vibrational relaxation have a great effect on nonequilibrium flowfields. Methods have been developed which account for the effect of vibrational nonequilibrium on the molecular dissociation rates, and for the effect of dissociation on vibrational relaxation.<sup>8,9</sup> One important difference between some of these methods is whether they

\* Graduate Research Assistant

\*\* Professor Aerospace Engineering, Associate Fellow AIAA

\*\*\* Visiting Assistant Professor, Member AIAA

assume that dissociation occurs with equal probability from all vibrational energy levels, or with a higher probability from higher energy levels. A nonpreferential model assumes that dissociation will occur with an equal probability from all vibrational energy levels, given a sufficiently energetic collision. On the other hand, a preferential model assumes that, given a sufficiently energetic collision, dissociation will occur with a higher probability from higher energy levels. Previous work<sup>7</sup> developed a modified nonpreferential model after Treanor and Marrone.<sup>8</sup> This model is referred to as the MCVDV model. However, some authors<sup>10, 11</sup> suggest that the preferential model should be more physically correct. In this paper, a preferential model is included in the flow solver following the preferential model developed by Marrone and Treanor.<sup>9</sup> This model will be referred to as the preferential MCVDV model.

### Flowfield Model

The VSL program developed previously<sup>1-4</sup> is used to solve for flowfield properties along the stagnation line between the shock and the body. All solutions presented are in an air mixture with eleven species and twenty-three reactions, as described in Ref. 4. The only changes made for this paper are to the vibration-dissociation coupling model, and to the absorption coefficients of some molecular band systems. These changes are described in more detail below.

### Vibration-Dissociation Coupling

The vibrational energy equation used in the VSL equations has the following form in Cartesian coordinates.

$$\begin{aligned} \rho u^j c_{p,v} \frac{\partial T_v}{\partial x^j} = & \frac{\partial}{\partial x^j} \left( \eta_v \frac{\partial T_v}{\partial x^j} \right) + \sum_s \rho_s U_s \frac{\partial h_{v,s}}{\partial x^j} \\ & + \sum_s \rho_s A \frac{e_{v,s}(T_v) - e_{v,s}}{\tau_v} + \sum_s \rho_s \frac{e_{v,s}(T_v) - e_{v,s}}{\tau_v} \\ & + \sum_s (e_{v,s} - E_s) \left( \frac{\partial p_s}{\partial t} \right)_f - \sum_s (e_{v,s} - G_s) \left( \frac{\partial p_s}{\partial t} \right)_b \end{aligned} \quad (1)$$

Vibration-vibration energy exchange rates between different vibrating molecules ( $N_2$ ,  $O_2$ ,  $NO$ , etc.) are not well known.<sup>12</sup> Therefore, only a single vibrational temperature has been used in the current model. An additional reason only one vibrational temperature has been used is the increased computational time associated with using different vibrational temperatures for each vibrating species.

The relaxation time,  $\tau_v$ , used in the current model is that proposed by Park<sup>13</sup> which sums the relaxation time used by Millikan and White<sup>14</sup>,  $\tau_v^{MW}$ , with a high temperature correction factor as follows

$$\tau_v = \tau_v^{MW} + \frac{1}{c_s \sigma_s N_s}$$

where  $c_s$  is the average species molecular speed and  $\sigma_s$  is a limiting cross section calculated by<sup>15</sup>

$$\sigma_s = 10^{-17} \left( \frac{50,000K}{T_v} \right)^2 \text{ cm}^2$$

The second relaxation time in Eq. 1, which only affects the  $N_2$  relaxation, is  $\tau_c$  and is taken from the work of Lee<sup>16</sup> as curve fitted by Candler and Park<sup>17</sup> as

$$\log(p_e \tau_c) = 7.50(\log T_e)^2 - 57.0 \log T_e + 98.70$$

for  $T_e < 7000K$ , and

$$\log(p_e \tau_c) = 2.36(\log T_e)^2 - 17.9 \log T_e + 24.35$$

for  $T_e \geq 7000K$ .

In the third term on the right side of Eq. (1), the factor  $A$  attempts to correct the relaxation rate for high temperature diffusion effects and is given by<sup>15</sup>

$$A = \left| \frac{T_{tr,sh} - T_v}{T_{tr,sh} - T_{v,sh}} \right| \left( 3.5 \exp \left( \frac{-5000K}{T_v} \right) - 1 \right)$$

The changes made in the MCVDV model described earlier affect only the last two terms in Eq. 1. The first of these terms represents the vibrational energy lost in dissociation, and the second term represents the vibrational energy gained in recombination. The derivation of these terms is shown below.

### Preferential MCVDV Model

In the nonpreferential model, a molecule involved in a collision with sufficient energy to cause dissociation will dissociate with equal probability from all vibrational energy levels. Of course, more dissociations will occur from the higher levels because less energy is required to reach the dissociation energy.

In the preferential model, molecules involved in collisions with sufficient energy to cause dissociation will have a greater probability of dissociating from higher vibrational energy levels. The probability of a molecule in the  $j$ th energy level dissociating is given by<sup>9</sup>

$$p_j = CF(j) N_j M(D - E_j) \quad (2)$$

where  $N_j$  is the fractional number of molecules with vibrational energy  $E_j$ ,  $M(D - E_j)$  represents the number of collisions with sufficient energy to cause dissociation,  $F(j)$  is proportional to the probability that a molecule in the  $j$ th vibrational energy level will dissociate given a sufficiently energetic collision, and  $C$  is a constant such that  $\sum p_j = 1$ .

$F(j)$  is assumed to be<sup>9</sup>

$$F(j) = \exp \left( \frac{-(D - E_j)}{kU} \right) \quad (3)$$

where  $U$  has dimensions of temperature and describes how quickly the probability of dissociation falls for low  $j$ . A value of  $U = \infty$  forces  $F(j) = 1$  and therefore corresponds to the nonpreferential model. Assuming a Boltzmann distribution in both the vibrational and translational modes,  $N_j$  and  $M(D - E_j)$  can be expressed as

$$N_j = \frac{\exp \left( \frac{-E_j}{kT_v} \right)}{Q(T_v)} \quad (4)$$

$$M(D - E_j) = \exp\left(\frac{-(D - E_j)}{kT_{tr}}\right) \quad (5)$$

Substituting Eq. 3 - 5 into Eq. 2 then gives for the probability of a dissociation from level  $j$

$$p_j = \frac{C}{Q(T_v)} \exp\left(\frac{-E_j}{kT_F}\right) \exp\left[\frac{-D}{k}\left(\frac{1}{U} + \frac{1}{T_{tr}}\right)\right] \quad (6)$$

with

$$\frac{1}{T_F} = \frac{1}{T_v} - \frac{1}{T_{tr}} - \frac{1}{U}$$

The requirement that  $\sum p_j = 1$  and the definition of the partition function then yields

$$C = \frac{Q(T_v)}{Q(T_F)} \exp\left[\frac{D}{k}\left(\frac{1}{U} + \frac{1}{T_{tr}}\right)\right]$$

Substituting this expression for  $C$  into Eq. 6 yields finally

$$p_j = \frac{\exp\left(\frac{-E_j}{kT_F}\right)}{Q(T_F)}$$

In Eq. 1,  $E_s$ , the amount of vibrational energy removed per dissociation, is then given by

$$E_s = \sum_j E_j p_j = \frac{\sum_j E_j \exp\left(\frac{-E_j}{kT_F}\right)}{Q(T_F)} \\ = kT_F^2 \frac{\partial}{\partial T_F} [\ln Q(T_F)]$$

The amount of vibrational energy gained per recombination is simply equal to  $E_s$  with  $T_v$  in equilibrium with  $T_{tr}$ . With  $T_v = T_{tr}$ ,  $T_F = -U$ . Therefore,  $G_s$  is given by

$$G_s = E_s(T_F = -U)$$

To obtain expressions for  $E_s$  and  $G_s$ , it is assumed that a simple harmonic oscillator models the vibrational energy. This is in contrast to Ref. 9, which used an anharmonic oscillator modeled by a Morse potential function. A simple harmonic oscillator is used here for computational simplicity. The differences between the simple harmonic oscillator and the anharmonic oscillator are also believed to have only a small effect for the flight conditions being investigated. The partition function for the simple harmonic oscillator is given by

$$Q(T_i) = \frac{1 - \exp\left(\frac{-\theta_v}{T_i}\right)}{1 - \exp\left(\frac{-\theta_v}{T_i}\right)}$$

Then, the expressions for  $E_s$  and  $G_s$  simplify to

$$E_s = \frac{\theta_v}{\exp\left(\frac{\theta_v}{T_F}\right) - 1} - \frac{\theta_v}{\exp\left(\frac{\theta_v}{T_F}\right) - 1} \\ G_s = \frac{\theta_v}{\exp\left(\frac{-\theta_v}{U}\right) - 1} - \frac{\theta_v}{\exp\left(\frac{-\theta_v}{U}\right) - 1}$$

The last term that is different for the preferential model is the vibrational coupling factor,  $V$ , which adjusts the dissociation rate constant,  $k_p$ , to account for the effect of vibrational nonequilibrium. This factor is derived in Ref. 9, and has the form

$$V = \frac{k_f}{k_{eq}} = \frac{Q(T_{tr})Q(T_F)}{Q(T_v)Q(-U)}$$

Table I. Summary of Test Cases

Case	R <sub>nose</sub> (cm)	V (km/s)	Altitude (km)	T <sub>wall</sub> (K)
1634	74.7	11.36	76.42	615
1636	74.7	11.31	71.04	810
1637.5	74.7	11.25	67.05	1030
1639	74.7	11.14	63.11	1325
1640.5	74.7	10.97	59.26	1560
14	230	14	80	1650

In all the above equations, setting  $U = \infty$  reduces the model to the nonpreferential model.

#### Radiation Model

The first order LTNE radiation model presented in Ref. 4 is used to calculate the radiative flux in the shock layer. However, experimental and theoretical studies by Laux and Kruger<sup>18</sup> and by Laux, Moreau, and Kruger<sup>19</sup> indicate that the normally accepted radiative transition probabilities for certain molecular bands are incorrect and need adjusting. Thus, as suggested in Ref. 18, the local thermodynamic equilibrium (LTE) absorption coefficients have been reduced in some of these studies by 10% for the  $N_2^+$  first negative system and the  $N_2$  second positive system, and by 15% for the  $N_2$  first positive system from the values in Ref. 4. Although Ref. 18 also suggests changes for the NO beta, gamma, and  $O_2$  Schumann-Runge bands, current studies of several flight conditions indicate that these changes have very little effect on the solution.

#### Discussion of Results

Table I gives a summary of the flight conditions investigated. The first five cases represent flight conditions at various times of the Fire 2 flight experiment. The first two flight times have significant amounts of nonequilibrium, while the last three contain progressively more equilibrium flow. The sixth case represents aerocapture conditions for a possible Martian return earth entry.

The freestream conditions and wall temperatures shown for the Fire 2 cases are those measured during the flight test at the times listed. The numerical solutions assume a fully catalytic wall boundary condition for the Fire 2 cases to be consistent with the beryllium heat shield used in the test vehicle and also include the radiative reflectance and absorption properties of the heat shield as a function of wavelength.

The last test case assumes the wall to be at 1650°K, which is the expected maximum temperature for a non-ablating heat shield. The solution assumes the surface for this case to be catalytic to ionic recombinations but

Table II. Summary of Results with  $U = D/3k$ 

Case	$\Delta$	$Q_c$	Coupled $Q_r$		
			Cont.	Lines	Absorbed
1634	5.77	188	13.4	4.97	12.4
1636	4.95	276	33.1	29.3	46.9
1637.5	4.68	356	56.2	67.1	93.3
1639	4.59	449	91.3	137	171
1640.5	4.53	538	120	220	248
14	13.8	57.9	61.5	44.3	106

$\Delta$  is shock standoff distance in cm.  
 $Q_c$  is convective heat transfer in watts/cm<sup>2</sup>.  
 $Q_r$  is radiative heat flux to wall in watts/cm<sup>2</sup>.  
 Lines and Continuum values are incident upon wall.

Table III. Summary of Results with  $U = 6D/k$ 

Case	$\Delta$	$Q_c$	Coupled $Q_r$		
			Cont.	Lines	Absorbed
1634	5.32	193	11.5	7.16	13.6
1636	4.69	281	29.6	31.4	46.9
1637.5	4.52	362	52.6	70.1	93
1639	4.47	444	82	133	161
1640.5	4.47	541	114	218	242
14	12.5	57	57.3	43.6	101

$\Delta$  is shock standoff distance in cm.  
 $Q_c$  is convective heat transfer in watts/cm<sup>2</sup>.  
 $Q_r$  is radiative heat flux to wall in watts/cm<sup>2</sup>.  
 Lines and Continuum values are incident upon wall.

non-catalytic to atomic recombinations and to be radiatively black.

The grid between the shock front and the body contains 99 points, which sufficiently resolves both nonequilibrium regions near the shock front and near the body. All cases assume shock slip conditions to conserve species and energy flux in the shock jump relations. A three temperature thermal model and a constant Lewis number diffusional model (with  $Le = 1.4$ ) have also been used.

For all flight conditions, varying degrees of preferentiality were studied. Values of  $U$  of  $D/6k$ ,  $D/3k$ ,  $D/k$ , and  $6D/k$  were used, with  $U=D/6k$  being the most preferential, and  $U=6D/k$  being practically nonpreferential. Solutions with  $U=6D/k$  and true nonpreferential solutions were only negligibly different. Therefore, this paper will assume that cases with  $U=6D/k$  are nonpreferential solutions. Also, all cases were run with both the reduced absorption coefficients and the nonreduced coefficients.

#### Preferential MCVDV Model

Table II summarizes results for the six cases with  $U=D/3k$ , which represents the amount of preferentiality recommended by Ref. 9. The first value in the table is the distance between the shock and the body,  $\Delta$ . The second value is the total convective heat transfer, consisting of the contributions from conduction, diffusion, and catalycity. Also listed is the total radiative heat transfer absorbed by the wall. The radiative heat transfer has been coupled with the gasdynamic solution. The table also includes a breakdown of the coupled radiative heat transfer into line and continuum contributions. The absorbed value is less than the sum of the line and continuum contributions for the Fire 2 cases because the surface is not a black body.

Table III contains the same information as Table II, but with  $U=6D/k$ . Tables II and III therefore compare preferential and nonpreferential solutions. For all cases, the shock standoff distance is increased for the preferential solution, while for most cases the convective heat transfer is

reduced or about the same. The continuum radiation is also higher for the preferential solutions, while the line contribution is lower for the earlier Fire 2 cases and slightly higher for the later times and for the 14 km/s case. The source of the decrease in the line contribution is currently being studied. The radiative flux absorbed is lower for the preferential case only for the earliest Fire 2 case. For the other cases, it is either unchanged or slightly higher. The probable reason for the slightly different behavior at different times of the Fire 2 cases is the amount of nonequilibrium in the flowfields of these cases. Since the earlier times contain significant amounts of nonequilibrium, the amount of preferentiality used has a significant effect on the solution. However, there is very little nonequilibrium present at the later times. Therefore, the amount of preferentiality used has only a mild effect on those solutions.

The differences in the flowfields for the preferential and nonpreferential solutions can be seen quite clearly in Fig. 1 and 2. Fig. 1 shows temperature and species concentration profiles for Fire 2 case 1634 with  $U=D/3k$ . Fig. 2 shows the same information with  $U=6D/k$ , a nonpreferential solution. Comparing the temperature profiles for the two cases, it is clear that the preferential solution increases the size of the nonequilibrium region behind the shock front. This behavior is expected for a preferential solution. Immediately behind the shock, the diatomic gases become vibrationally excited, and the molecules in the upper vibrational energy levels quickly dissociate due to the preferentiality, which leaves very few molecules in the upper vibrational energy levels. The molecules in the lower levels are much less likely to dissociate, reducing the dissociation rates. The lower dissociation rates in turn lengthen the vibrational relaxation times. Thus, the overall nonequilibrium region is lengthened.

The species concentration profiles in Fig. 1 and 2 also reflect the increased nonequilibrium region in the preferential case behind the shock front, particularly in the

$N_2$  and  $O_2$  profiles. The concentration of  $N_2^+$  is also especially important, since it is a very strong radiator. The peak concentration of  $N_2^+$  occurs farther away from the shock front for the preferential solution than for the nonpreferential solution. This movement is caused by the lower dissociation rates and increased relaxation times of the preferential solution. Although the magnitude of the peak concentration of  $N_2^+$  is nearly the same for both the preferential and the nonpreferential solutions, a high concentration of  $N_2^+$  exists over a larger spatial region of the shock layer for the preferential case. Thus, the total concentration of  $N_2^+$  in the shock layer is greater for the preferential solution. The effect of this increased concentration can be seen in Fig. 3 and 4, which show the spectral content of the wall radiation for the preferential and nonpreferential solutions of the 1634 case. The lower of the two plots in these figures is a detailed representation of the spectral radiative content. The upper plot uses line groupings over widths of the spectrum to show the summed contributions. The most obvious difference in these two plots is the increased radiation in the 2-4 eV range for the preferential case. The primary radiators in this range are  $N_2^+$ ,  $N_2$ , and NO. Since the strongest of these radiators is  $N_2^+$ , its increased concentration is the main cause of the increased radiation in the 2-4 eV range and the increased continuum contribution seen in Tables II and III.

Fig. 5-8 present solutions of case 1634 with  $U=D/6k$  and  $U=D/k$  to show the effect of differing amounts of preferentiality. Fig. 5 and 6 show that increasing the preferentiality further increases the nonequilibrium region and the continuum contribution in the 2-4 eV range. Fig. 7 and 8 show that decreasing the amount of preferentiality decreases the nonequilibrium region and the continuum contribution in the 2-4 eV range, though they are still greater than the nonpreferential solution.

Fig. 9 compares the Fire 2 solutions with  $U=D/3k$  with the experimental data. The Fire 2 experiment contained three different heat transfer measurements. A total calorimeter measured the sum of the convective heat transfer and the absorbed radiative flux, which is shown on the figure as a solid line. Experimental values for the total calorimeter were not available above 1639 sec. as this is when the first heat shield began to melt. The corresponding numerical results are shown as squares. The other two gauges measured radiative intensity in the frequency ranges of 0.02 to 6.2 eV and 2 to 4 eV, respectively, from which the radiative heating can be computed assuming the gas to be optically thin. The first range covers most of the spectrum from low infrared through the visible range and is shown on the figure as a dashed line labeled  $Q_r$  (0.02 - 6.2 eV). The corresponding numerical results are shown as diamonds. The second range is a region consisting primarily of molecular band radiation of  $N_2^+$  and NO. The experimental data in the 2 - 4 eV range was scattered over a large area,

and is bounded by two dashed lines on the figure labeled  $Q_r$  (2 - 4 eV). The numerical results in this range are represented by circles. Also, all Fire 2 experimental values presented have been adjusted by the effective view factor of 0.84.

Fig. 10 shows the same information as Fig. 9 for a nonpreferential solution. Comparing Fig. 9 and 10, both the preferential and the nonpreferential solutions match the Fire 2 data reasonably well for the total heat transfer. For the preferential solution, percent errors range from 14 % at 1634 to 6.9 % at 1639. In the 0.02 - 6.2 and 2 - 4 eV ranges, however, the agreement with the flight data is not as good. At the early flight times, all the numerical results appear high. However, the preferential solution is significantly higher in the 2 - 4 eV range, with percent errors ranging from 165 % at 1634 sec. to 1.7 % at 1640.5 sec. The percent error of the nonpreferential solution is 64 % at 1634 sec., with the last three data points within the range of the experimental scatter. This behavior is due, once again, to the higher concentration of  $N_2^+$  for the preferential solution. In the 0.02 - 6.2 eV range, both solutions are about 42 % below the experimental values at the higher times. However, at the earlier flight times, the preferential solution is higher than the nonpreferential solution. Thus, the nonpreferential solution is more consistently low compared with the experimental results.

Returning for a moment to Tables II and III, there appears to be some inconsistency in the results at the higher flight times. At 1640.5, there is an increase in the continuum and line contributions and in the absorption for the preferential case, where at the lower times there was a decrease in the line contribution and in the absorption. This apparent inconsistency can be somewhat explained by viewing Fig. 11, which shows the temperature profiles and radiation spectrum for the preferential solution of Fire 2 case 1640.5. First of all, the temperature profile shows that the nonequilibrium region is very small, indicating that preferentiality has very little effect on equilibrium solutions. Tables II and III also illustrate this point, as the largest difference between the values in these tables at 1640.5 is a 5 % increase in the continuum contribution for the preferential case. A possible reason for some of the inconsistency at the higher times can be seen in the lower half of Fig. 11, which has a much different scale than the other radiation spectra shown. At this time, the contribution from the 2 - 4 eV range is a small percentage of the overall radiation. Therefore, changes in the radiation from the ultraviolet range could be having a greater effect on the solution than the changes in the 2 - 4 eV range. However, the exact nature of the changes in the ultraviolet range is not yet known, but is under investigation.

While the Fire 2 cases sufficiently illustrate the effects of preferentiality, a few comments can also be made about the AOTV 14 km/s case. Comparing the values listed

Table IV. Summary of Results with  $U = D/3k$  and Reduced Absorption Coefficients

Case	$\Delta$	$Q_c$	Coupled $Q_r$		
			Cont.	Lines	Absorbed
1634	5.78	188	13.6	6.21	12
1636	4.94	275	34.3	32.2	45.3
1637.5	4.68	355	55.1	69.3	92.9
1639	4.59	449	89.9	137	171
1640.5	4.54	539	119	221	248
14	13.8	59	61.3	44.9	106

$\Delta$  is shock standoff distance in cm.  
 $Q_c$  is convective heat transfer in watts/cm<sup>2</sup>.  
 $Q_r$  is radiative heat flux to wall in watts/cm<sup>2</sup>.  
 Lines and Continuum values are incident upon wall.

Table V. Summary of Results with  $U = 6D/k$  and Reduced Absorption Coefficients

Case	$\Delta$	$Q_c$	Coupled $Q_r$		
			Cont.	Lines	Absorbed
1634	5.17	187	8.92	5.19	9.87
1636	4.69	279	28	30.1	46.5
1637.5	4.52	360	50.6	68.4	92.1
1639	4.48	446	82.2	134	162
1640.5	4.49	534	116	225	249
14	12.4	56.4	54.5	42.1	96.5

$\Delta$  is shock standoff distance in cm.  
 $Q_c$  is convective heat transfer in watts/cm<sup>2</sup>.  
 $Q_r$  is radiative heat flux to wall in watts/cm<sup>2</sup>.  
 Lines and Continuum values are incident upon wall.

in Tables II and III for this case, similarities to the later Fire 2 times can be seen. There is an increase in the continuum and line contributions and in the absorption for the preferential case, similar to the later Fire 2 times. However, Fig. 12 - 15 show that there is a significant amount of nonequilibrium for the 14 km/s case. Fig. 12 and 13 are a preferential solution while Fig. 14 and 15 are a nonpreferential solution. Once again, an increased nonequilibrium region behind the shock front can be seen for the preferential case, particularly in the  $N_2$  and  $O_2$  profiles. Also, notice that the radiation spectra are plotted on a different scale than the Fire 2 radiation spectra. The same increase in the contribution from the 2 - 4 eV range can be observed for the preferential case, and again is most likely due to an increase in the  $N_2^+$  concentration. However, the source of the increased line contribution is unclear.

The comparisons of the numerical solutions with the Fire 2 data and the apparent inconsistencies among various cases illustrate that the amount of preferentiality has a complex effect on the solution. The reasons for this complex behavior is not currently well understood and needs further study.

#### Reduced Absorption Coefficients

The same cases described above were also run with the absorption coefficients of the  $N_2^+$  first negative,  $N_2$  first positive, and  $N_2$  second positive systems reduced as described earlier. A summary of these results is shown in Tables IV and V. Table IV lists results for preferential solutions while Table V lists results for nonpreferential solutions. The comparisons between the preferential and nonpreferential solutions without the reduced absorption coefficients also apply for the solutions with the reduced absorption coefficients. The only difference appears to be that the line contribution is slightly higher for the preferential solution even at the earlier Fire 2 times, whereas for the nonreduced absorption coefficient cases the

line contribution at the earlier times was slightly lower for the preferential cases. In general, though, the effect of preferentiality is the same for these cases.

The effect of reducing the absorption coefficients is not very clearly seen by comparing Tables IV and V with Tables II and III. There appear to be several inconsistencies between the nonreduced and the reduced solutions. For the preferential cases, the continuum contribution of the reduced coefficient cases is slightly higher for the earlier times, but slightly lower for the later times. The line contributions of the reduced coefficient cases are slightly higher or unchanged for all times, while the absorbed wall radiation is slightly lower for the earlier times and unchanged for the later times.

The trends are significantly different for the nonpreferential solutions. Here, the continuum contribution of the reduced coefficient cases is significantly lower at the earlier times, but slightly higher at the later times. This behavior is exactly the opposite from the preferential solutions. The line contribution and the absorbed heat transfer in the reduced coefficient cases are lower at the earlier times, but slightly higher at the later times. Any reductions in the continuum contributions should be primarily due to the reduced  $N_2^+$  first negative absorption coefficient. Obviously, the preferentiality has a very complex effect on any solution, and this effect is made even more complex by changes in absorption coefficients.

Fig. 16 and 17 show temperature and species profiles and radiation spectrums for nonpreferential Fire 2 case 1634 with the reduced absorption coefficients. Comparing these figures with Fig. 2 and 4, it is clear that reducing the absorption coefficients has very little effect on the gasdynamic solution. On the other hand, the effect on the radiation spectra is obvious. The magnitude of the radiation in the 2 - 4 eV range is considerably lower for the reduced absorption coefficient case, further proof that the

reduction in the continuum contribution is primarily due to the reduced  $N_2^+$  first negative absorption coefficient.

Fig. 18 and 19 show the same information for a preferential solution with  $U=D/3k$ . Comparing these figures with Fig. 1 and 3, the same comments made for the nonpreferential solution also apply here. However, the magnitude of the effect of reducing the absorption coefficients appears to be smaller, indicating that the preferentiality has a stronger effect on the solution than reducing the absorption coefficients.

Fig. 20 compares the nonpreferential solution with the reduced absorption coefficients with the Fire 2 flight measurements. Comparing this figure with Fig. 9 and 10, the agreement with the experiment seems better with the reduced absorption coefficients. While the contribution in the 2 - 4 eV range is still high at the early flight time, it is not as high as before, with percent errors ranging from 40 % to 27 % at the earliest flight times. At the later flight times, the numerical data is within the range of the experimental scatter. Once again, the numerical results in the 0.02 - 6.2 eV range appear to be consistently low, with percent errors at the higher flight times around 45 %. However, at the earlier flight times, the reduced absorption coefficient results match the experimental results more closely than the nonreduced solutions. There does not appear to be much difference in the total heat transfer calculations. Since most of the total is convective heating, reducing the absorption coefficients does not have a large effect on the total heating.

For the AOTV 14 km/s case, the differences between the reduced and nonreduced coefficient cases also show some interesting behavior. For the preferential case, the convective heating increases slightly with the reduced coefficients. However, the convective heating decreases slightly with the reduced coefficients for the nonpreferential case. Other changes are also apparent in other values from Tables II - V for the 14 km/s case, further illustrating that more investigating needs to be conducted on the effects of preferentiality.

#### Conclusions

A preferential MCVDV model has been developed and evaluated by comparisons with a nonpreferential MCVDV model. The preferential solutions exhibit the proper behavior compared with the nonpreferential solutions. However, comparisons with Fire 2 flight measurements indicate better agreement with the nonpreferential model. A preferential temperature of  $U=D/3k$  also appears to introduce too large an amount of preferentiality into the solution for Fire 2 cases. A slightly larger value such as  $U=D/k$  may be more appropriate.

Solutions were also obtained using reduced absorption coefficients for the first negative band of  $N_2^+$  and for the first and second positive bands of  $N_2$ . Comparisons with Fire 2 flight measurements for these solutions are

encouraging, indicating that better calculations of radiative transition probabilities need to be included. However, the nonpreferential model still matches the flight measurements better than the preferential model. More investigations in the modeling of the  $N_2^+$  first negative band may be needed. In all computations, this band is always very near LTE. If this is not true, the continuum contribution in the 2 - 4 eV range would be lowered at the earlier Fire 2 flight times, which have significant nonequilibrium.

Although the preferential model should be more physically correct than the nonpreferential model, current results indicate that little if any preferentiality is present in the Fire 2 flight conditions. Therefore, some modifications to the preferential model may be in order. Also, there are likely still questions concerning the modeling of some molecular LTNE and other radiative phenomena and research in these areas is continuing. It would appear that more theoretical and numerical studies in high temperature, nonequilibrium radiative phenomena are needed.

#### Acknowledgment

This work was primarily supported by NASA Grant NAG-1-1003 from the Langley Research Center, with Dr. Lin C. Hartung as technical monitor.

#### References

- <sup>1</sup> Carlson, L. A. and Gally, T. A., "The Effect of Electron Temperature and Impact Ionization on Martian Return AOTV Flowfields," *Journal of Thermophysics and Heat Transfer*, vol.5, No. 1, January 1991, pp. 9-20.
- <sup>2</sup> Carlson, L. A. and Gally, T. A., "Nonequilibrium Chemical and Radiation Coupling Phenomena in AOTV Flowfields," AIAA Paper 91-0569, January 1991.
- <sup>3</sup> Gally, T. A., Carlson, L. A. and Green, D., "A Flowfield Coupled Excitation and Radiation Model for Nonequilibrium Reacting Flows," AIAA Paper 91-1463, June 1991.
- <sup>4</sup> Gally, T. A. and Carlson, L. A., "An Approximate Local Thermodynamic Nonequilibrium Radiation Model for Air," AIAA Paper 92-2972, July 1992.
- <sup>5</sup> Thompson, R. A., "Comparison of Nonequilibrium Viscous Shock Layer Solutions with Windward Shuttle Heating Data," AIAA Paper 87-1473, June 1987.
- <sup>6</sup> Nicolet, W. E., "Advanced Methods for Calculating Radiation Transport in Ablation-Product Contaminated Boundary Layers," NASA CR 1656, September, 1970.

<sup>7</sup> Nicolet, W. E., "Rapid Methods for Calculating Radiation Transport in the Entry Environment," NASA CR 2528, April 1975.

<sup>8</sup> Treanor, C.E. and Marrone, P.V., "Effect of Dissociation on the Rate of Vibrational Relaxation," *Physics of Fluids*, vol. 5, No. 9, September, 1962, pp.1022-1026.

<sup>9</sup> Marrone, P.V. and Treanor, C.E., "Chemical Relaxation with Preferential Dissociation from Excited Vibrational Levels," *Physics of Fluids*, vol. 6, No. 9, September, 1963, pp.1215- 1221.

<sup>10</sup> Treanor, C. E. and Marrone, P. V., "Vibration and Dissociation Coupling Behind Strong Shock Waves," *Dynamics of Manned Lifting Planetary Entry*, edited by S. M. Scala, John Wiley and Sons, New York, 1963, pp. 160-171.

<sup>11</sup> Gnoffo, P. A., Gupta, R. M. and Shinn, J. L. "Conservation Equations and Physical Models for Hypersonic Air Flows in Thermal and Chemical Nonequilibrium", NASA TP 2867, February 1989.

<sup>12</sup> Park, C., *Nonequilibrium Hypersonic Aerothermodynamics*, John Wiley & Sons, New York, 1990, pp.166-167.

<sup>13</sup> Park, C., "Calculation of Nonequilibrium Radiation in the Flight Regimes of Aeroassisted-Orbital Transfer Vehicles," *Thermal Design of Aeroassisted Orbital Transfer Vehicles*, Progress in Astronautics and Aeronautics, vol. 96, Ed. H.F. Nelson, AIAA 1985, pp.395-418.

<sup>14</sup> Millikan, R.C. and White, D.R., "Systematics of Vibrational Relaxation," *Journal of Chemical Physics*, vol. 39, No. 12, December, 1963, pp.3209-3213.

<sup>15</sup> Park, C., "Assessment of Two Temperature Kinetic Model for Ionizing Air," AIAA Paper 87-1574, June 1987.

<sup>16</sup> Lee, J.H., "Electron-Impact Vibrational Excitation Rates in the Flowfield of Aeroassisted Orbital Transfer Vehicles," *Thermal Design of Aeroassisted Orbital Transfer Vehicles*, Progress in Astronautics and Aeronautics, vol. 96, Ed. H.F. Nelson, AIAA 1985, pp.197-224.

<sup>17</sup> Candler, G. and Park, C., "The Computation of Radiation from Nonequilibrium Hypersonic Flows," AIAA Paper 88-2678, June 1988.

<sup>18</sup> Laux, C. and Kruger, C., "Arrays of Radiative Transition Probabilities for the N<sub>2</sub> First and Second Positive, NO Beta and Gamma, N<sub>2</sub><sup>+</sup> First Negative, and O<sub>2</sub> Schumann-Runge Band Systems," *J. Quant. Spectrosc. Radiat. Transfer*, vol. 48, No. 1, pp.9-24, 1992.

<sup>19</sup> Laux, C., Morcau, S. and Kruger, C., "Experimental Study and Improved Modeling of High-Temperature Air Radiation," AIAA Paper 92-2969, July 1992.

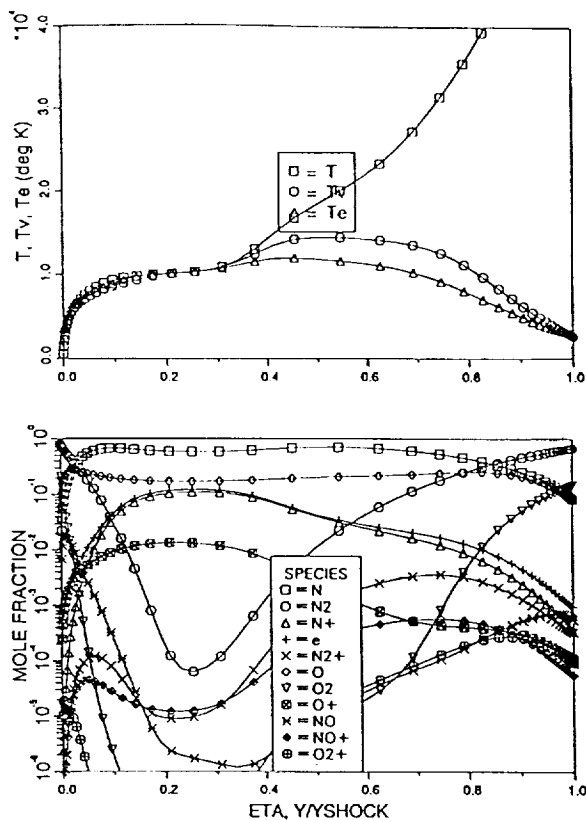


Fig. 1: Case 1634 - Air Results with  $U = D/3k$ , Temperature and Mole Fractions

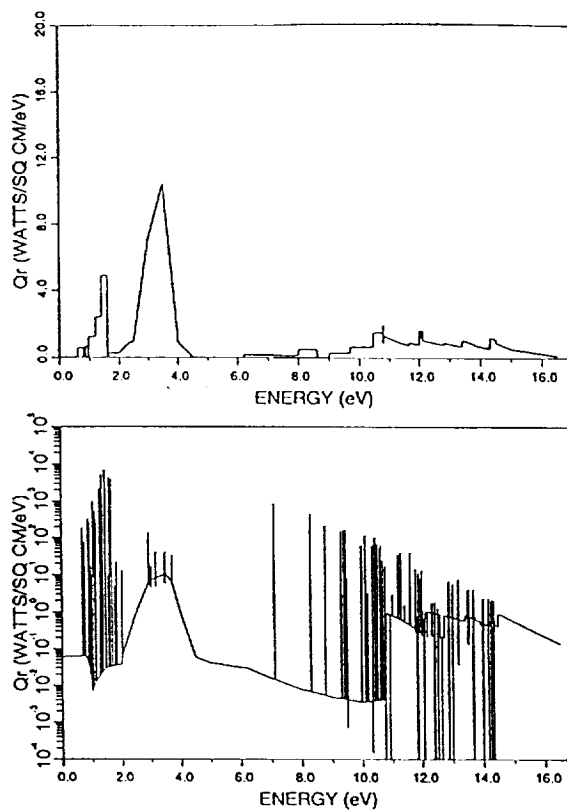


Fig. 3: Case 1634 - Air Results with  $U = D/3k$ , Grouped and Detailed Radiation Spectra

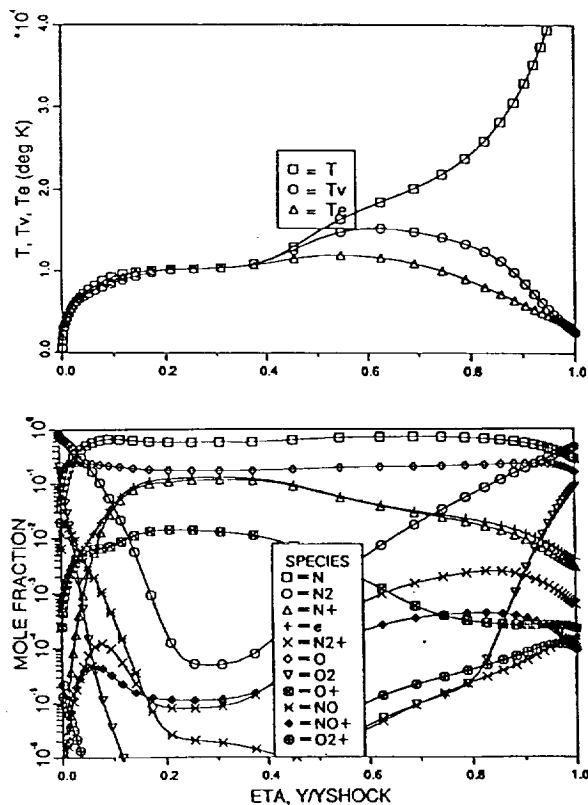


Fig. 2: Case 1634 - Air Results with  $U = 6D/k$ , Temperature and Mole Fractions

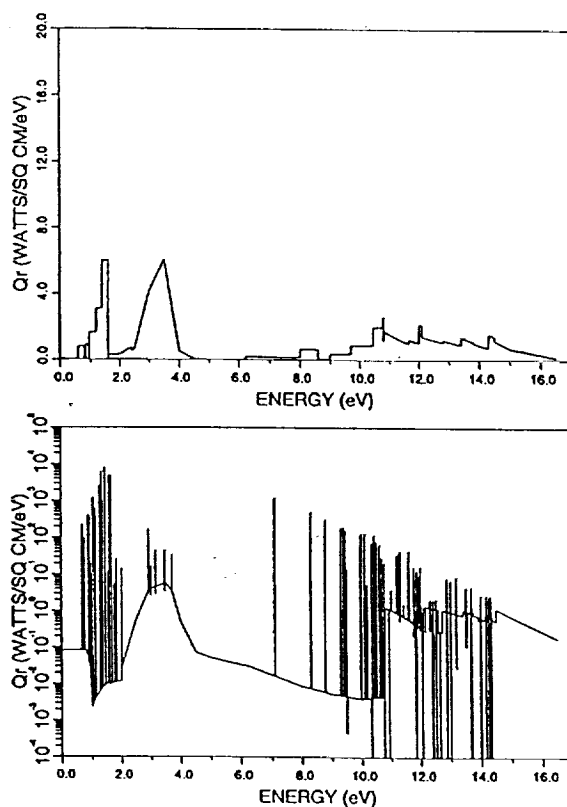


Fig. 4: Case 1634 - Air Results with  $U = 6D/k$ , Grouped and Detailed Radiation Spectra

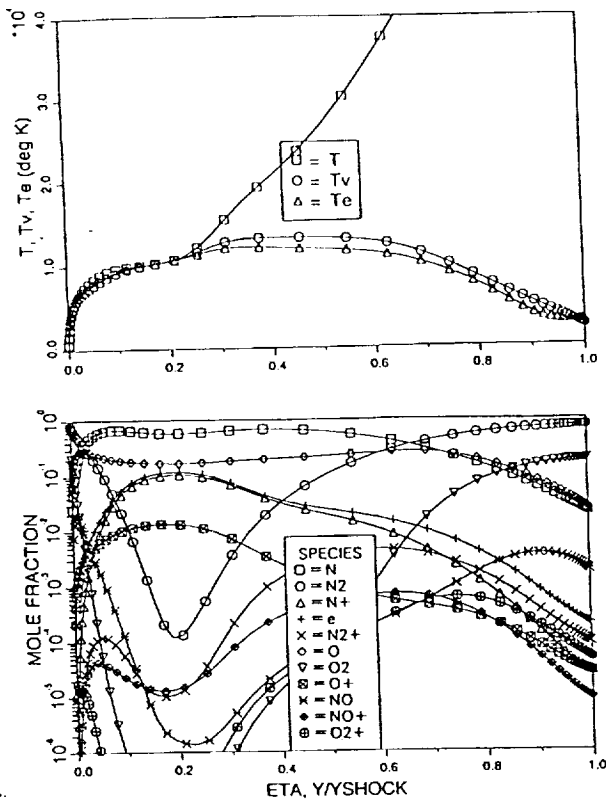


Fig. 5: Case 1634 - Air Results with  $U = D/6k$ , Temperature and Mole Fractions

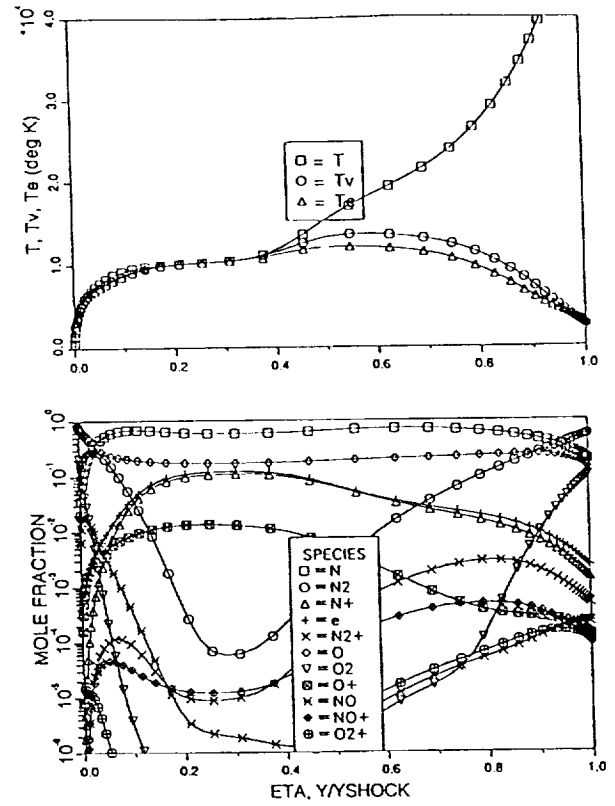


Fig. 7: Case 1634 - Air Results with  $U = D/k$ , Temperature and Mole Fractions

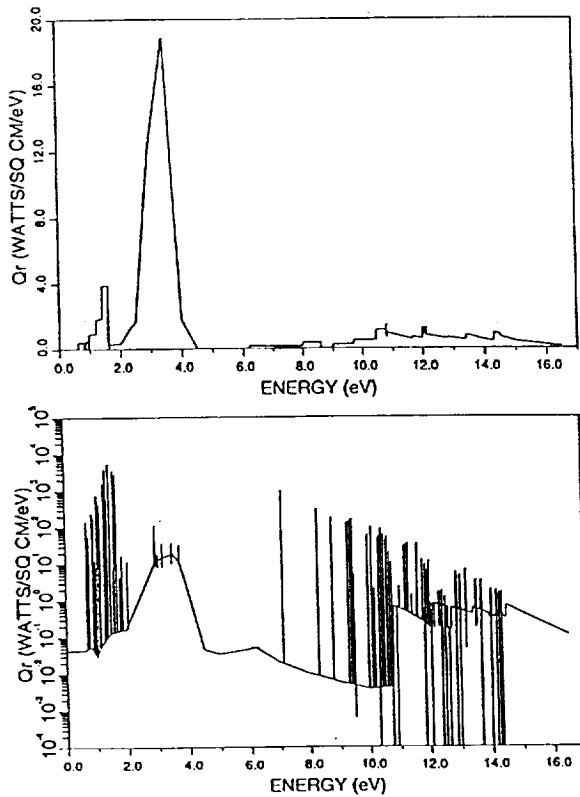


Fig. 6: Case 1634 - Air Results with  $U = D/6k$ , Grouped and Detailed Radiation Spectra

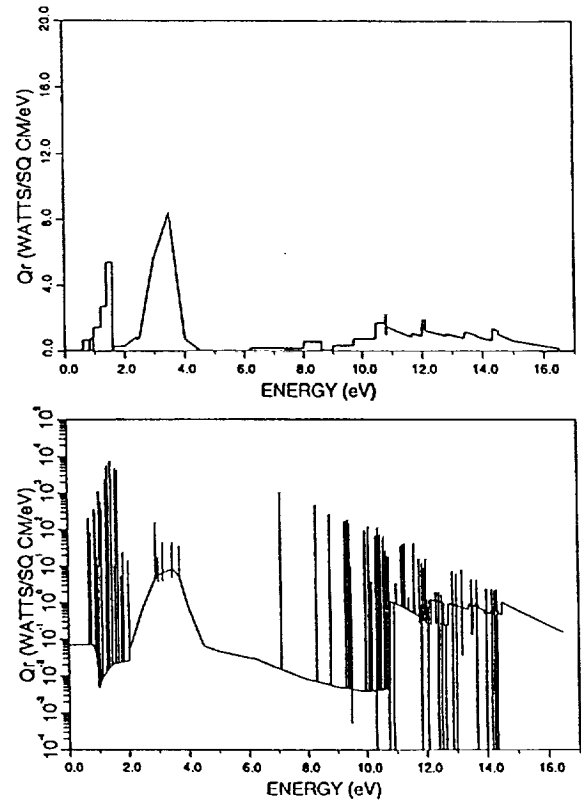


Fig. 8: Case 1634 - Air Results with  $U = D/k$ , Grouped and Detailed Radiation Spectra

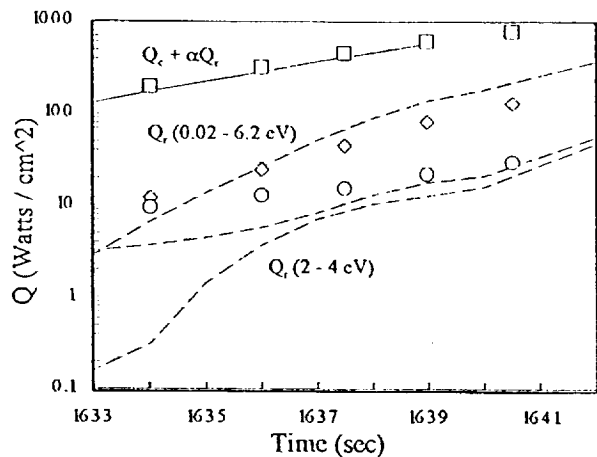


Fig. 9: Comparison of Preferential Model ( $U=D/3k$ ) With Fire 2 Flight Test Measurements

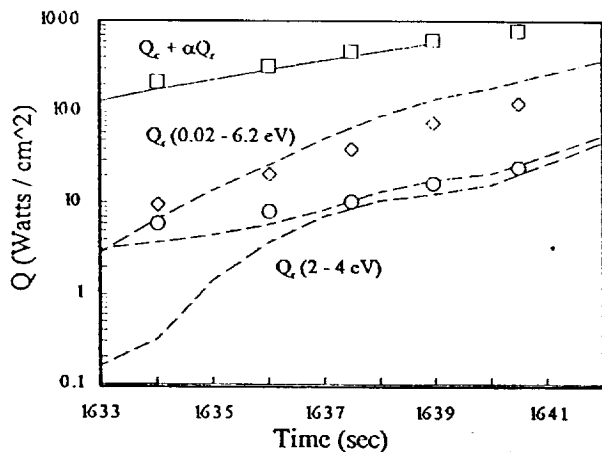


Fig. 10: Comparison of Nonpreferential Model With Fire 2 Flight Test Measurements

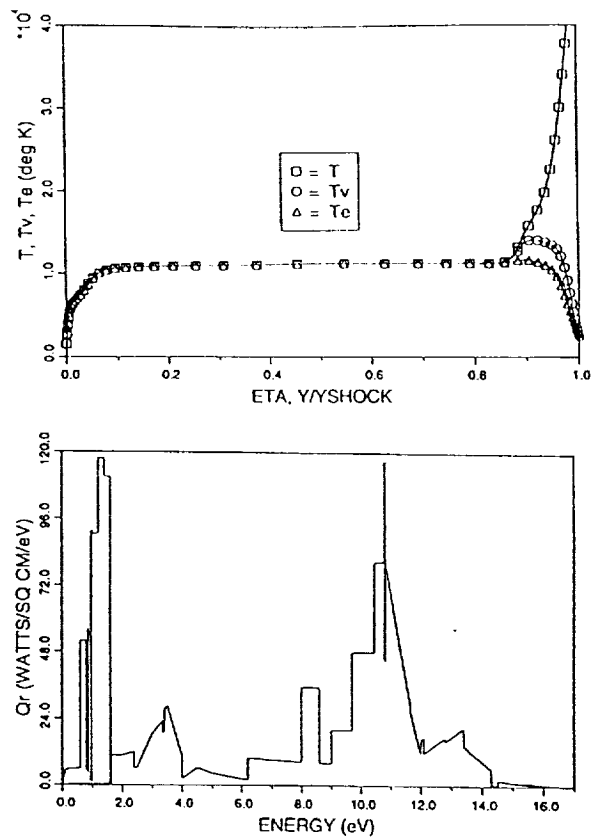


Fig. 11: Case 1640.5 - Air Results with  $U = D/3k$ , Temperature and Grouped Radiation Spectra

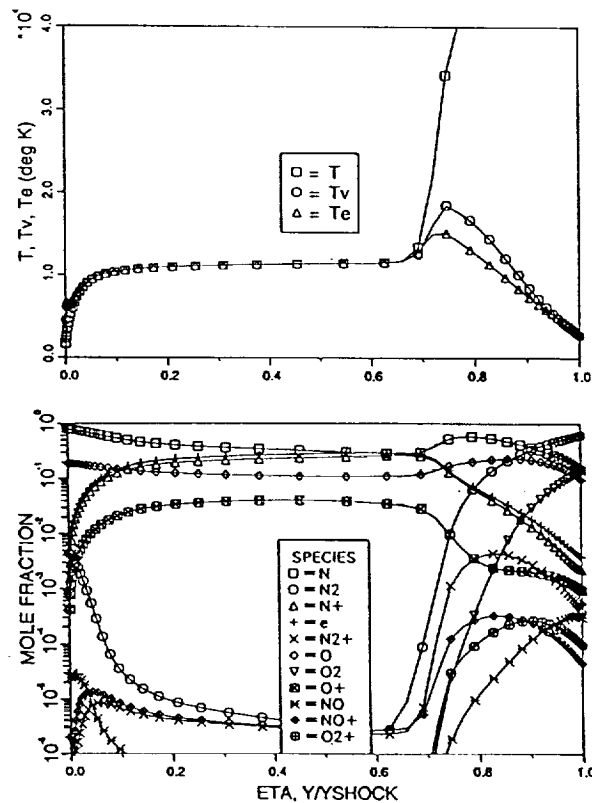


Fig. 12: Case 14 - Air Results with  $U = D/3k$ , Temperature and Mole Fractions

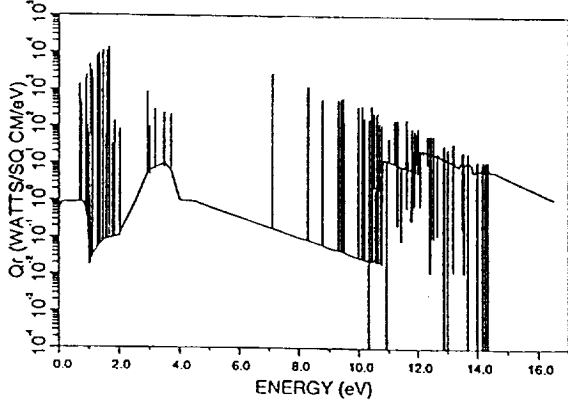
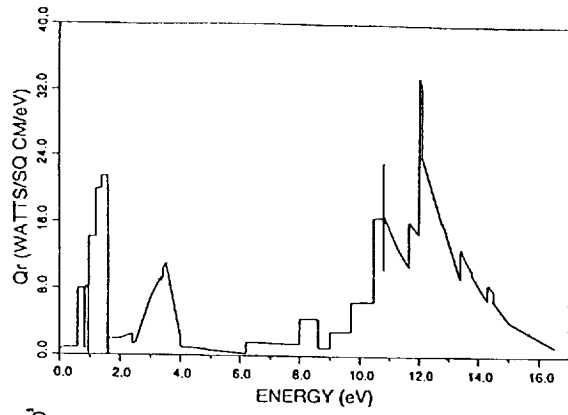


Fig. 13: Case 14 - Air Results with  $U = D/3k$ , Grouped and Detailed Radiation Spectra

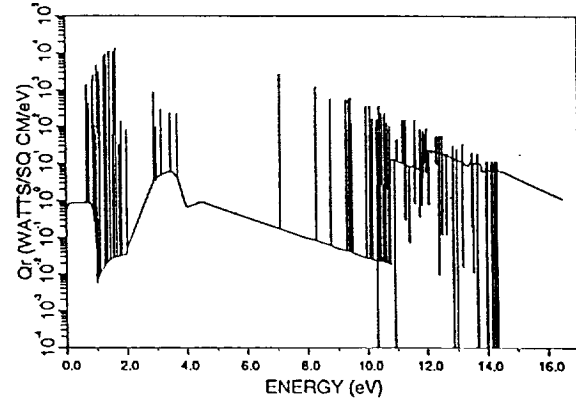
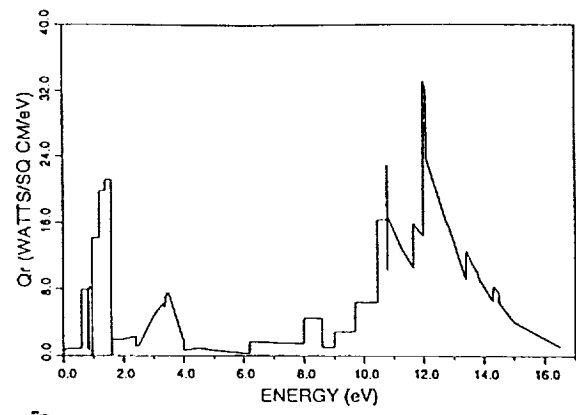


Fig. 15: Case 14 - Air Results with  $U = 6D/k$ , Grouped and Detailed Radiation Spectra

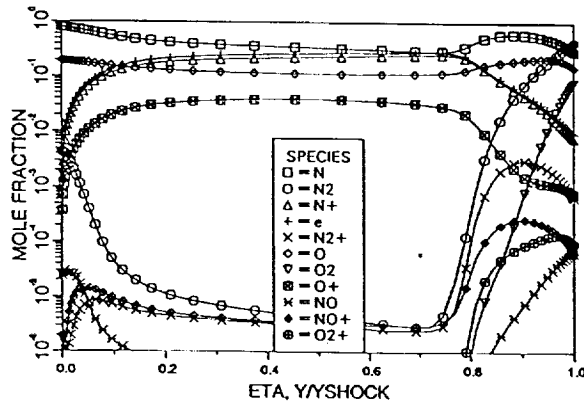
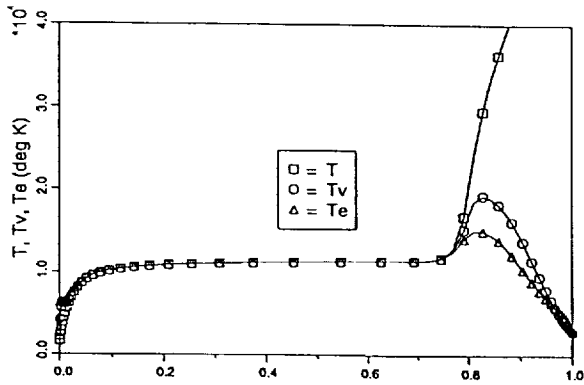


Fig. 14: Case 14 - Air Results with  $U = 6D/k$ , Temperature and Mole Fractions

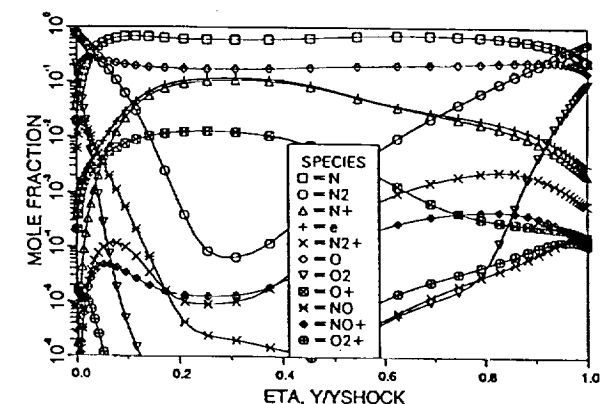
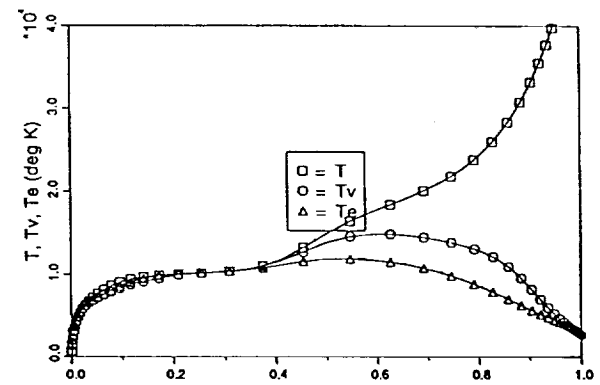


Fig. 16: Case 1634 - Air Results with  $U = 6D/k$ , Reduced Absorption Coefficients, Temperature and Mole Fractions

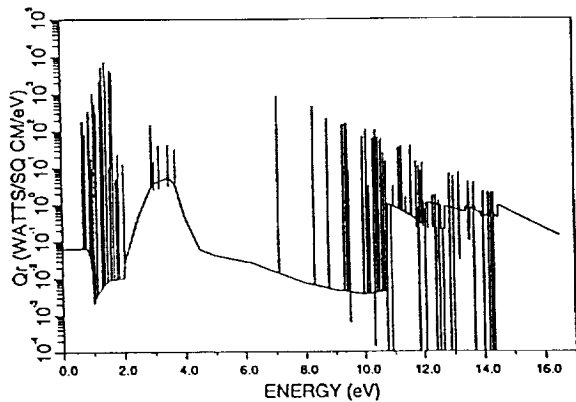
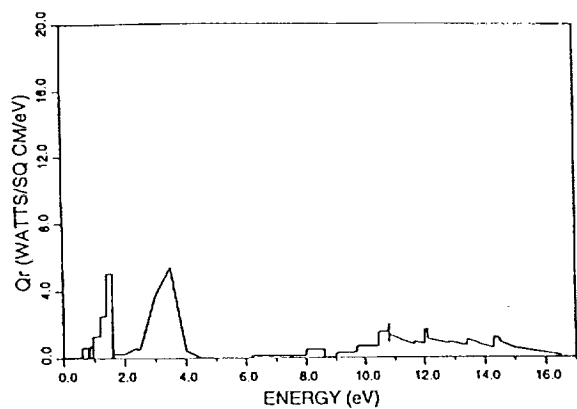


Fig. 17: Case 1634 - Air Results with  $U = 6D/k$ , Reduced Absorption Coefficients, Grouped and Detailed Radiation Spectra

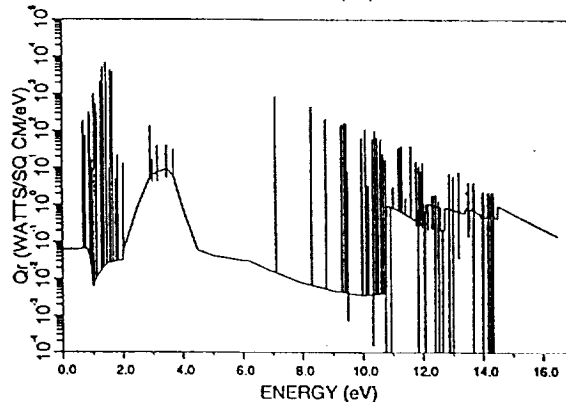
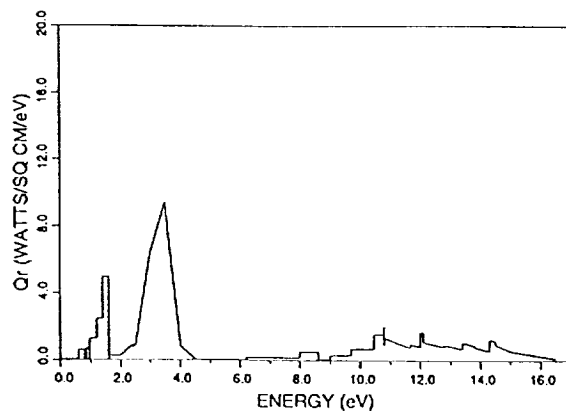


Fig. 19: Case 1634 - Air Results with  $U = D3/k$ , Reduced Absorption Coefficients, Grouped and Detailed Radiation Spectra

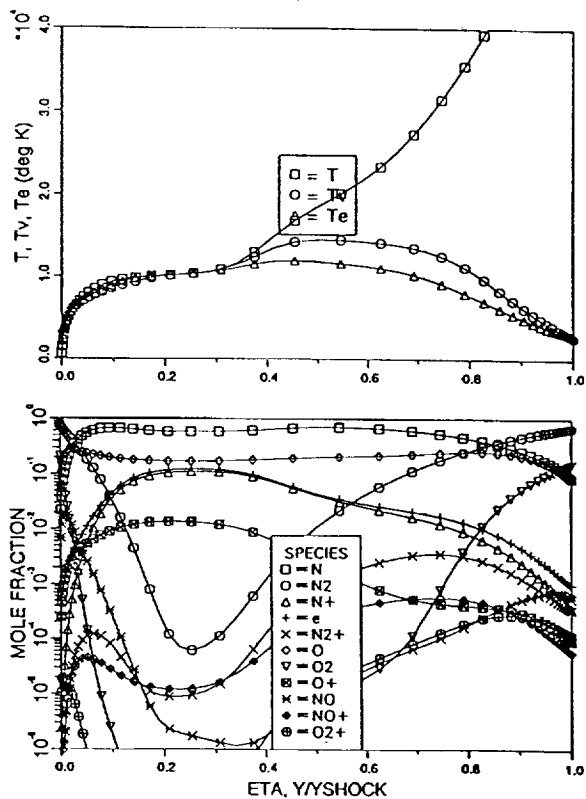


Fig. 18: Case 1634 - Air Results with  $U = D/3k$ , Reduced Absorption Coefficients, Temperature and Mole Fractions

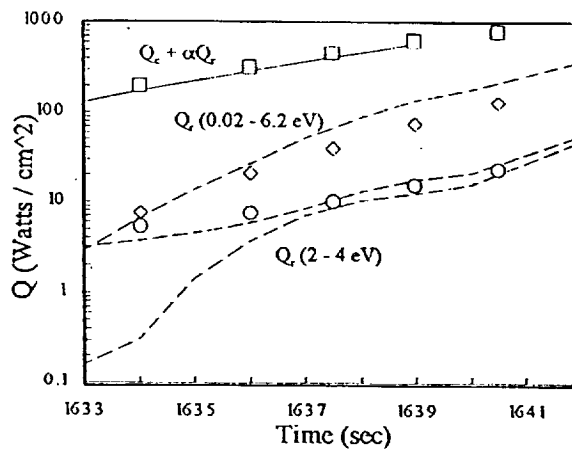


Fig. 20: Comparison of Nonpreferential Model With Reduced Absorption Coefficients With Fire 2 Flight Test Measurements